nature neuroscience

ARTICLES

Reduced sensory synaptic excitation impairs motor neuron function via Kv2.1 in spinal muscular atrophy

Emily V Fletcher[1,2], Christian M Simon[1,2], John G Pagiazitis[1,2], Joshua I Chalif[1,2], Aleksandra Vukojicic[1,2], Estelle Drobac[1,2], Xiaojian Wang[1,2] & George Z Mentis[1–3]

Behavioral deficits in neurodegenerative diseases are often attributed to the selective dysfunction of vulnerable neurons via cell-autonomous mechanisms. Although vulnerable neurons are embedded in neuronal circuits, the contributions of their synaptic partners to disease process are largely unknown. Here we show that, in a mouse model of spinal muscular atrophy (SMA), a reduction in proprioceptive synaptic drive leads to motor neuron dysfunction and motor behavior impairments. In SMA mice or after the blockade of proprioceptive synaptic transmission, we observed a decrease in the motor neuron firing that could be explained by the reduction in the expression of the potassium channel Kv2.1 at the surface of motor neurons. Chronically increasing neuronal activity pharmacologically *in vivo* led to a normalization of Kv2.1 expression and an improvement in motor function. Our results demonstrate a key role of excitatory synaptic drive in shaping the function of motor neurons during development and the contribution of its disruption to a neurodegenerative disease.

Movement is an essential behavior that is controlled by motor circuits. The intricate assembly of motor circuits is established by genetic programs[1] and is subsequently refined by synaptic activity[2]. Within spinal motor circuits, motor neurons (MNs) bridge the central and peripheral nervous systems by conveying central commands to the skeletal muscles. MNs receive synapses from sensory neurons[3], spinal interneurons[4] and supraspinal pathways[5]. However, the underlying mechanisms of how neurotransmission shapes MN output are undefined. Furthermore, genetic perturbations causing neurodegenerative diseases may lead to synaptic and circuit dysfunction and initiate the demise of normal behavior.

In neurodegenerative diseases, behavioral impairment is attributed to the dysfunction of a specific neuronal type that is distinctly vulnerable to a ubiquitous gene mutation[6]. Dysfunction of select neurons acting as the primary targets of disease-causing mutations may precipitate secondary changes in their synaptic partners and exacerbate the disease[7]. Whether and how neuronal dysfunction in principally affected neurons may cause dysfunction of their synaptic partners and influence pathogenesis has not been established.

Here we used a mouse model of SMA, an inherited neurodegenerative disease, to investigate the impact of non-cell-autonomous mechanisms in the pathogenesis of disease. SMA is characterized by MN death, muscle atrophy and motor impairment[8]. Patients have homozygous mutations in the ubiquitously expressed gene survival motor neuron 1 (*SMN1*), but retain copies of a nearly identical hypomorphic gene *SMN2* (refs. 9,10), causing SMN protein deficiency[10]. SMN dysfunction in neurons, but not in muscles, underlies motor impairment in mouse[11] and fly[12] SMA models. We have shown that synaptic dysfunction occurs simultaneously with MN hyperexcitability, preceding MN death[13]. Whether synaptic dysfunction is responsible for the MN hyperexcitability or synaptic loss occurs in response to MN dysfunction is unresolved. The primary neuronal target(s) affected by SMN deficiency leading to SMA motor circuit dysfunction remain elusive.

We report that SMA MNs increase their input resistance but exhibit decreased firing as a result of sensory–motor synapse dysfunction. Strikingly, both characteristics of MN dysfunction are rescued by selective SMN restoration in proprioceptive neurons. Further, synaptic dysfunction is characterized by impaired glutamate release, accompanied by a reduction of Kv2.1 channel expression in SMA MNs. The reduction of Kv2.1 is reversed by SMN restoration in proprioceptive neurons or by pharmacologically induced increase in network activity. Our findings elucidate cellular and network mechanisms responsible for SMA pathology and identify sensory excitatory synaptic drive as a major determinant in regulating MN output.

RESULTS

MN dysfunction onset correlates with proprioceptive synaptic impairment in SMA

SMA MNs exhibit selective vulnerability depending on the muscles they innervate, with proximal muscles more affected than distal muscles in mice[14] and humans[15]. We previously reported that SMA MNs in the first lumbar segment (L1) exhibit an increase in input resistance early in the disease[13]. Whether vulnerable SMN-deficient MNs become dysfunctional as a result of synaptic impairment or due to MN-autonomous mechanisms is unknown. To study vulnerable MNs, we focused on those that innervate the iliopsoas (IL) and quadratus lumborum (QL) muscles[13,14]. These muscles are involved in posture

[1]Center for Motor Neuron Biology and Disease, Columbia University, New York, New York, USA. [2]Department of Pathology and Cell Biology, Columbia University, New York, New York, USA. [3]Department of Neurology, Columbia University, New York, New York, USA. Correspondence should be addressed to G.Z.M. (gzmentis@columbia.edu).

Received 27 June 2016; accepted 4 April 2017; published online 15 May 2017; doi:10.1038/nn.4561

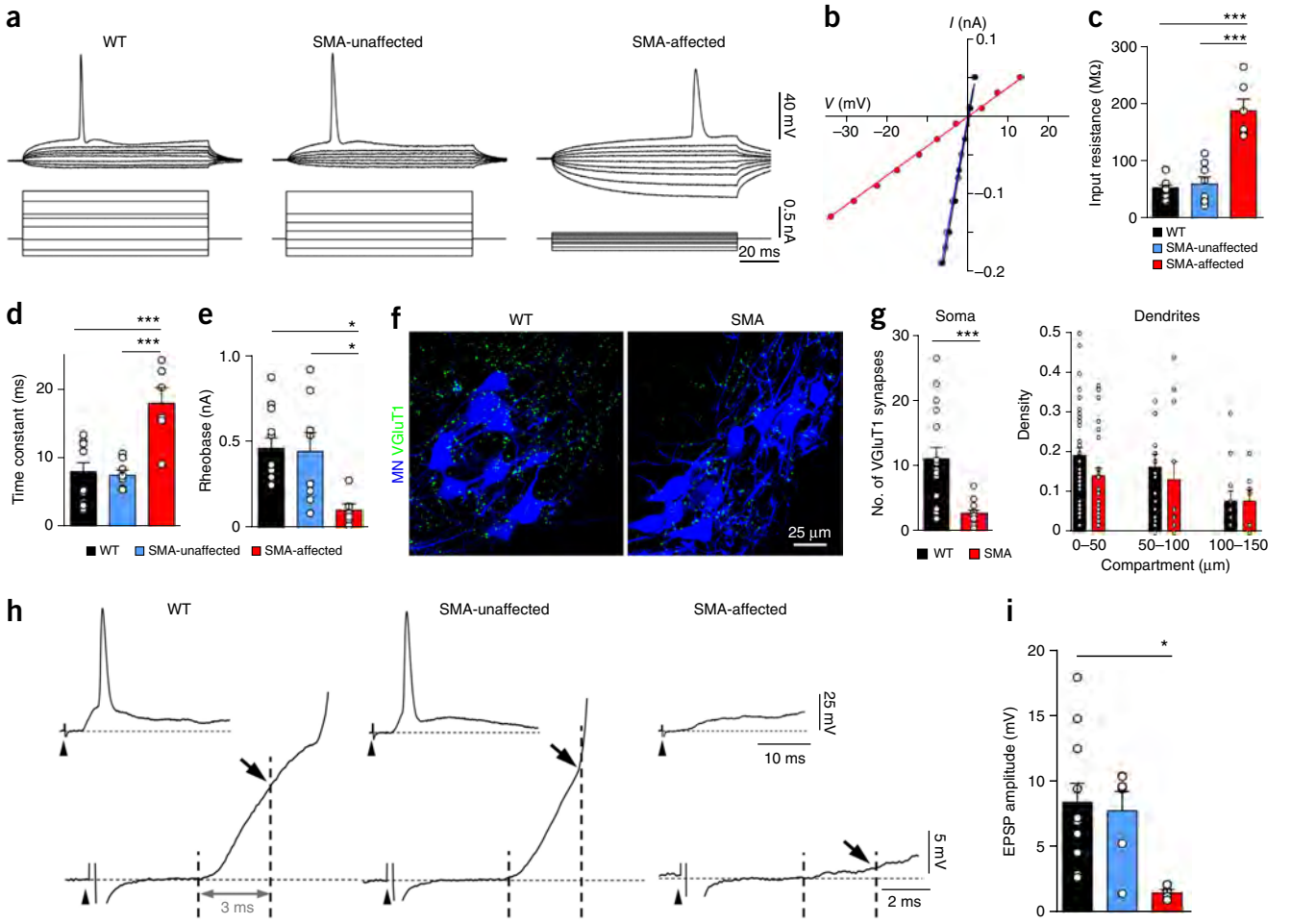

Figure 1 Early dysfunction in a subset of vulnerable SMA MNs. (**a**) Membrane responses (top) following current injection (bottom) in a WT, an SMA-unaffected and an SMA-affected MN. (**b**) Current/voltage relationship for a WT (black), an SMA-unaffected (blue) and an SMA-affected (red) MN. (**c**) Average input resistance for WT ($n = 12$), SMA-unaffected ($n = 8$) and SMA-affected ($n = 6$) MNs at P2. One-way ANOVA, Tukey's *post hoc* analysis, $^{***}P < 0.001$. (**d**) The average time constant for WT ($n = 12$), SMA-unaffected ($n = 8$) and SMA-affected ($n = 6$) MNs. One-way ANOVA, Tukey's *post hoc* analysis, $^{***}P < 0.001$. (**e**) Average rheobase for WT ($n = 12$), SMA-unaffected ($n = 8$) and SMA-affected ($n = 6$) MNs. One-way ANOVA, Tukey's *post hoc* analysis ($^{*}P = 0.004$, WT versus SMA-affected; $^{*}P = 0.006$, SMA-unaffected versus SMA-affected). (**f**) *z*-stack projection of confocal images from retrogradely labeled L2 MNs (blue) and VGluT1 synaptic boutons (green) in a WT and an SMA mouse at P2. The total distance in the *z* axis for each was 7 µm (20 optical planes at 0.35-µm intervals). (**g**) The average number of VGluT1 boutons on the entire soma (left) and synaptic dendritic density (right) in 50-µm dendritic compartments from the soma, for WT ($n = 17$) and SMA ($n = 13$) MNs. $^{***}P < 0.001$, unpaired *t*-test (soma); not significant for dendrites, *t*-test for 0–50 µm ($P = 0.09$) and Mann–Whitney for 50–100 ($P = 0.24$) and 100–150 µm ($P = 0.95$) dendritic compartments. (**h**) Intracellular responses after supramaximal stimulation of the L2 dorsal root in a WT, SMA-unaffected and SMA-affected MN at P2 (insets). The monosynaptic part of the EPSP is shown on an expanded timescale for each neuron (vertical dotted lines). Arrows indicate the maximum EPSP amplitude and arrowheads the stimulus artifact. (**i**) Average EPSP peak amplitude for WT ($n = 11$), SMA-unaffected ($n = 6$) and SMA-affected ($n = 4$) MNs. One-way ANOVA, Tukey's *post hoc* analysis ($^{*}P = 0.02$, WT versus SMA-affected). All data are represented as mean ± s.e.m. For details, see **Supplementary Methods Checklist**.

and locomotion[15] and in the righting reflex, which is impaired in SMA mouse models[13]. The IL/QL MNs reside within the L1 to L3 spinal segments[16]. Tracing experiments from muscle together with ventral root L2 dye fill[13] indicated that most IL/QL MNs lie laterally within the L2 spinal segment (**Supplementary Fig. 1**).

The excitability of a neuron is defined by its ability to generate action potentials in response to injected currents or synaptic inputs and is regulated by its intrinsic membrane properties. To study the intrinsic passive and active membrane properties and monosynaptic sensory-induced synaptic potentials of L2 MNs, we made whole-cell current clamp recordings in an intact mouse spinal cord *ex vivo* preparation[13] at postnatal day (P) 2 (**Supplementary Fig. 2a**). Analysis of the intrinsic membrane properties of SMA MNs revealed two populations (**Supplementary Fig. 2b**). 57% were similar to wild-type (WT) MNs ("SMA-unaffected"), while 43% exhibited signs of dysfunction ("SMA-affected"), evidenced by increased input resistance and time constant and reduced rheobase (**Fig. 1a–e**). To investigate whether resistant SMA MNs were also affected, we studied L5 lateral MNs, which innervate the gastrocnemius and tibialis anterior, distal hindlimb muscles, at P4. We found no difference in the intrinsic membrane properties of WT and SMA L5 MNs even at this later stage of the disease (**Supplementary Fig. 2c–e**). Thus, ubiquitous SMN deficiency in MNs does not cause dysfunction in all spinal MNs, further highlighting the selective vulnerability of specific MN pools.

To determine the basis of MN dysfunction in L2 SMA-affected MNs, we first quantified the number of proprioceptive synapses on

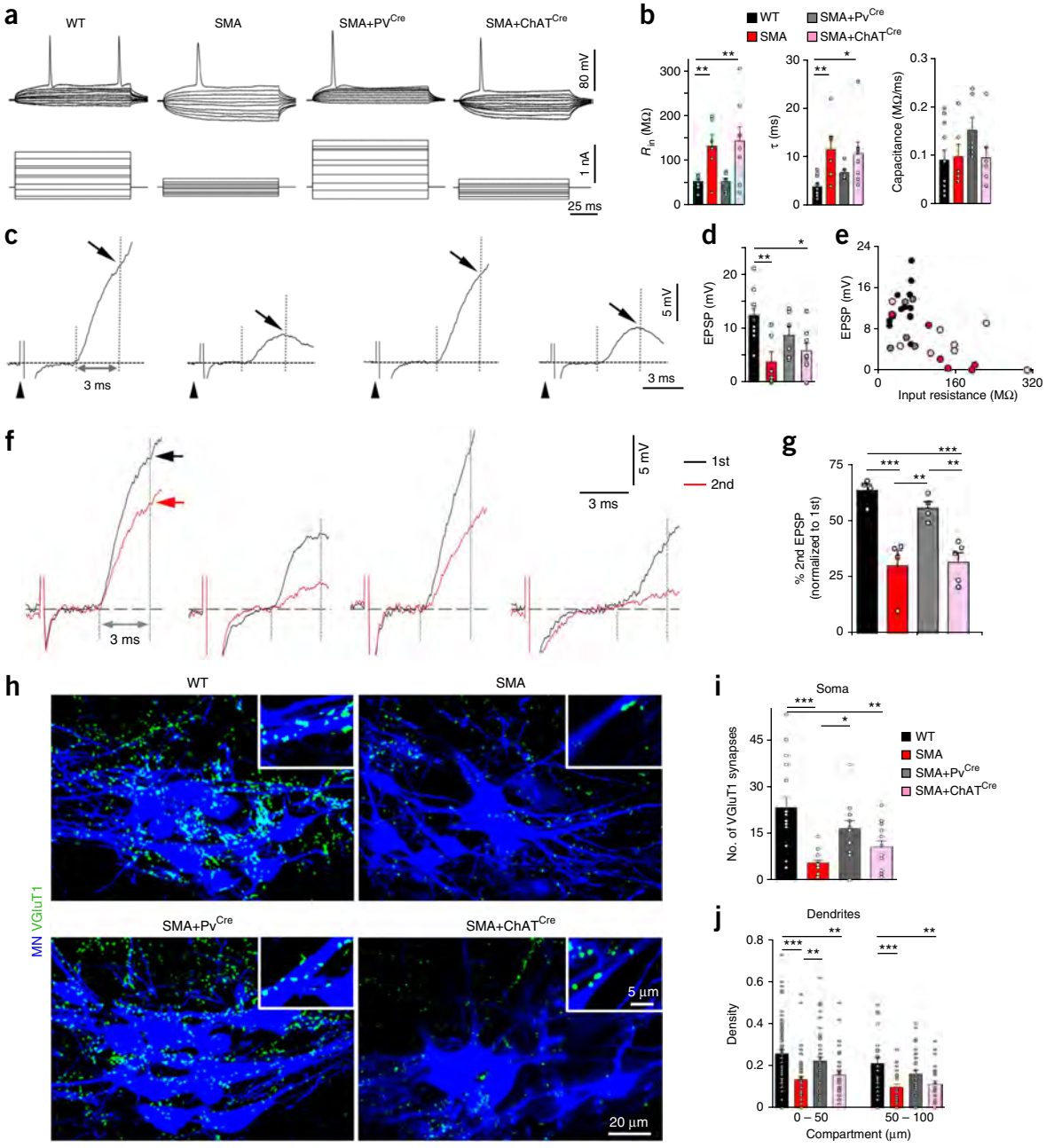

Figure 2 Selective upregulation of SMN in proprioceptive neurons alone normalizes MN membrane hyperexcitability and VGluT1 synapses. (**a**) Membrane responses (top) following current injection (bottom) in WT, SMA, SMA+Pv^{Cre} and SMA+ChAT^{Cre} L2 MNs at P4. (**b**) The average input resistance (R_{in}), membrane time constant (τ) and capacitance in WT ($n = 11$), SMA ($n = 6$), SMA+Pv^{Cre} ($n = 6$) and SMA+ChAT^{Cre} ($n = 8$) L2 MNs. One-way ANOVA, Tukey's *post hoc* analysis ($^{*}P = 0.0159$, $^{**}P < 0.01$). (**c**) Intracellular responses of monosynaptic EPSPs following supramaximal stimulation of the L2 dorsal root in homonymous MNs for the same groups shown in **a**. Arrows indicate the peak EPSP amplitude measured at 3 ms after the onset of response and arrowheads the stimulus artifact. (**d**) The average peak EPSP amplitude in MNs for the groups shown in **c**. One-way ANOVA, Tukey's *post hoc* analysis ($^{*}P = 0.0060$, $^{**}P = 0.0006$). (**e**) Relationship between peak EPSP amplitude and input resistance of L2 MNs for the groups shown in **a**. (**f**) First (black) and second (red) EPSP responses elicited in MNs after 1-Hz dorsal root stimulation in the groups shown in **a**. Arrows indicate the peak EPSP amplitude measured at 3 ms after the onset of response. (**g**) Average percentage of second EPSP response, normalized to first response, by MNs in the groups shown in **f**. One-way ANOVA, Tukey's *post hoc* analysis ($^{**}P < 0.01$, $^{***}P < 0.001$). (**h**) *z*-stack projection of confocal images from retrogradely labeled L2 MNs (blue) and VGluT1 synaptic boutons (green) in a WT, SMA, SMA+Pv^{Cre} and SMA+ChAT^{Cre} mouse at P4. Insets show VGluT1 synaptic appositions on dendrites at higher magnification. The total distance in the *z* axis for all main panels was 7 µm (20 optical planes at 0.35-µm intervals) and for the insets 1.5 µm. (**i**) The average number of VGluT1 boutons on somata of L2 WT ($n = 17$), SMA ($n = 14$), SMA+Pv^{Cre} ($n = 13$) and SMA+ChAT^{Cre} ($n = 15$) MNs. One-way ANOVA, Tukey's *post hoc* analysis ($^{***}P < 0.0001$, $^{**}P = 0.002$ and $^{*}P = 0.021$). (**j**) VGluT1 synaptic density on 50 µm dendritic compartments from the soma, for the same groups shown in **h**. One-way ANOVA, Tukey's *post hoc* analysis (0–50 µm: $^{***}P < 0.0001$, WT versus SMA; $^{**}P = 0.001$, WT versus SMA+ChAT^{Cre} and $^{**}P = 0.008$, SMA versus SMA+Pv^{Cre}; 50–100 µm: $^{***}P = 0.0007$, WT versus SMA; $^{**}P = 0.005$, WT versus SMA+ChAT^{Cre}). All data are represented as mean ± s.e.m. For details, see **Supplementary Methods Checklist**.

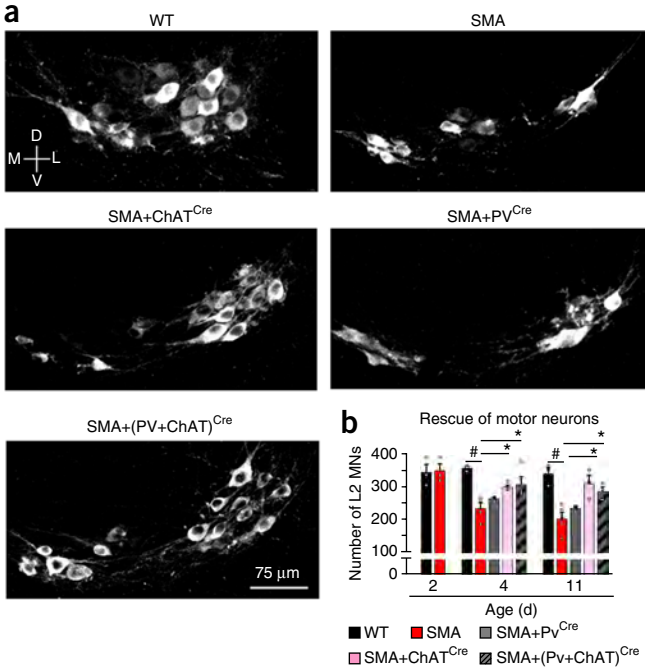

Figure 3 MN loss due to SMN deficiency is mediated by cell-autonomous mechanisms. (**a**) Confocal images of WT ($n = 3$), SMA ($n = 4$), SMA+Pv^{Cre} ($n = 3$), SMA+ChAT^{Cre} ($n = 4$) and SMA+(Pv+ChAT)^{Cre} ($n = 4$) L2 MNs visualized by ChAT immunoreactivity at P4. (**b**) Time course (P2–P11) of the total number of L2 MNs for the experimental groups shown in **a**. All data are represented as mean ± s.e.m. One-way ANOVA, Tukey's *post hoc* analysis, $^{\#}P < 0.05$ versus WT and $^{*}P < 0.05$ versus SMA. For details, see **Supplementary Methods Checklist**.

their somata and proximal dendrites. We employed retrograde tracing to label the somatodendritic tree of MNs[13] together with immunohistochemistry against vesicular glutamate transporter 1 (VGluT1) (**Fig. 1f**), a marker of proprioceptive synapses[17]. We found a modest overall reduction in VGluT1 synapses on the SMA MNs, and there was no synaptic loss on dendrites (**Fig. 1g**), where over 90% of the proprioceptive synapses make contact with MNs[13,18]. Furthermore, analysis of the number of VGluT1 synapses, plotted against the transverse surface area of the MN soma, revealed that all SMA L2 MNs were equally affected (**Supplementary Fig. 2h**,**i**). Thus, the loss of proprioceptive synapses on the soma is unlikely to be the main contributor to increased input resistance in SMA MNs.

Next we analyzed the monosynaptically induced excitatory postsynaptic potential (EPSP) following proprioceptive fiber stimulation. While SMA-unaffected MNs exhibited comparable EPSP amplitudes to WT MNs, SMA-affected hyperexcitable MNs exhibited reduced EPSPs (**Fig. 1h**,**i**). Resistant L5 SMA MNs exhibited similar EPSP amplitudes to WT (**Supplementary Fig. 2f**,**g**). These results highlight a strong relationship between synaptic function and intrinsic membrane properties of MNs, suggesting that synaptic dysfunction precedes synaptic loss and induces an increase in MN input resistance early in disease.

Loss of SMN from proprioceptive neurons weakens sensory–motor synapses and causes MN dysfunction

To define the cellular basis of sensory–motor circuit dysfunction in SMA, we restored SMN specifically in proprioceptive neurons, specifically in MNs, or in both neuronal classes in SMA mice. We used a mouse model of SMA harboring a single targeted mutation and two transgenic alleles, resulting in the genotype *Smn*$^{Res/+}$;*SMN2*$^{+/+}$;*SMNΔ7*$^{+/+}$ (where *Smn* is used for the mouse *Smn1* gene and *SMN* for the human *SMN2* gene) (ref. 19). The allele carrying the targeted mutation (*Smn*^{Res}) is engineered to revert to a fully functional *Smn* allele upon Cre-mediated recombination (*Cre*$^{+/-}$;*Smn*$^{Res/-}$;*SMN2*$^{+/+}$;*SMNΔ7*$^{+/+}$)[19]. *SMN2* is the human gene and *SMNΔ7* corresponds to the human *SMN* cDNA lacking exon 7. In the absence of the Cre recombinase (*Cre*$^{-/-}$;*Smn*$^{Res/-}$;*SMN2*$^{+/+}$;*SMNΔ7*$^{+/+}$) the phenotype of these mice is similar to that of the *SMNΔ7* SMA mice[19], and this approach has been validated in several studies[19–21].

Restoration of SMN protein in proprioceptive neurons was achieved by crossing the conditional inversion SMA mice with Pv^{Cre} mice, which express Cre under the control of the parvalbumin (*Pvalb*) promoter. Parvalbumin is expressed exclusively in proprioceptive neurons during the first 10 postnatal days[22] and was expressed similarly in WT and SMA mice (**Supplementary Fig. 3a**,**b**). Parvalbumin was expressed in the cerebellum at P5 (**Supplementary Fig. 3a**,**b**), and behaviors known to depend on cerebellar activity, including postural control and balance, do not become efficient until ~P14 in neonatal rats[23] and are unlikely to have a major effect during the first postnatal week. Experimentally, transection at a high medulla level revealed that cerebellar activity did not significantly affect the righting reflex of P3 WT mice ($P = 0.20$; **Supplementary Fig. 3c**,**d**). Additionally, SMA-vulnerable slow twitch muscles such as the QL[24] did not express parvalbumin (**Supplementary Fig. 4**). The same results were observed in Pv^{Cre}::lsl-TdTomato (where lsl is *loxP*-STOP-*loxP*) mice (**Supplementary Fig. 5**). We restored SMN in MNs by crossing the conditional inversion SMA mice with those expressing Cre under the choline acetyltransferase (*Chat*) promoter (SMA+ChAT^{Cre}). To investigate Cre efficacy, we crossed the Pv^{Cre} and ChAT^{Cre} with lsl-TdTomato mice; 95% of ChAT^{+} MNs expressed TdTomato and 91% of parvalbumin^{+} neurons in the dorsal root ganglion expressed TdTomato (**Supplementary Fig. 6a**,**b**). Immunohistochemistry against Cre revealed that 89% of ChAT^{+} MNs expressed Cre in ChAT^{Cre} mice and 87% of Pv^{+} proprioceptive neurons expressed Cre in Pv^{Cre} mice (**Supplementary Fig. 6c**,**d**). To examine the efficacy and specificity of SMN upregulation following Cre recombination in proprioceptive and MNs, we used SMN immunohistochemistry to study the presence of Gems, nuclear structures containing SMN[25], in proprioceptive and MNs in the L2 spinal segment at P4 (**Supplementary Fig. 6e–h**). We found 93% of WT proprioceptive neurons expressed Gems, compared to none in SMA and 60% in SMA+Pv^{Cre} mice (**Supplementary Fig. 6g**). Similarly, 81% of MNs in WT mice expressed Gems and 50% in SMA+ChAT^{Cre} mice (**Supplementary Fig. 6h**), confirming selective SMN restoration in the majority of proprioceptive and MNs.

To address the cellular origin of the increased input resistance of SMA MNs, we investigated the effects of selective SMN restoration in either proprioceptive neurons or MNs at P4. At this age, ~85% of SMA MNs exhibited an increase in input resistance and time constant (**Fig. 2a**,**b**), revealing a progressive pathology in L2 SMA MN function over the first neonatal week. Ruling out a reduction in soma size as an explanation for the increased input resistance, measurements of whole-cell capacitance revealed no differences between WT and SMA MNs (**Fig. 2b**). Furthermore, comparison of the soma size from WT and SMA MNs, filled with neurobiotin during intracellular recordings, revealed no statistical difference (**Supplementary Fig. 7a–d**). Strikingly, the increased input resistance of SMN-deficient MNs was corrected to WT levels in SMA+Pv^{Cre} mice, while restoration of SMN in only MNs (SMA+ChAT^{Cre}) had no effect (**Fig. 2a**,**b**). Therefore, increased input resistance of SMA MNs is mediated by non-cell-autonomous mechanisms.

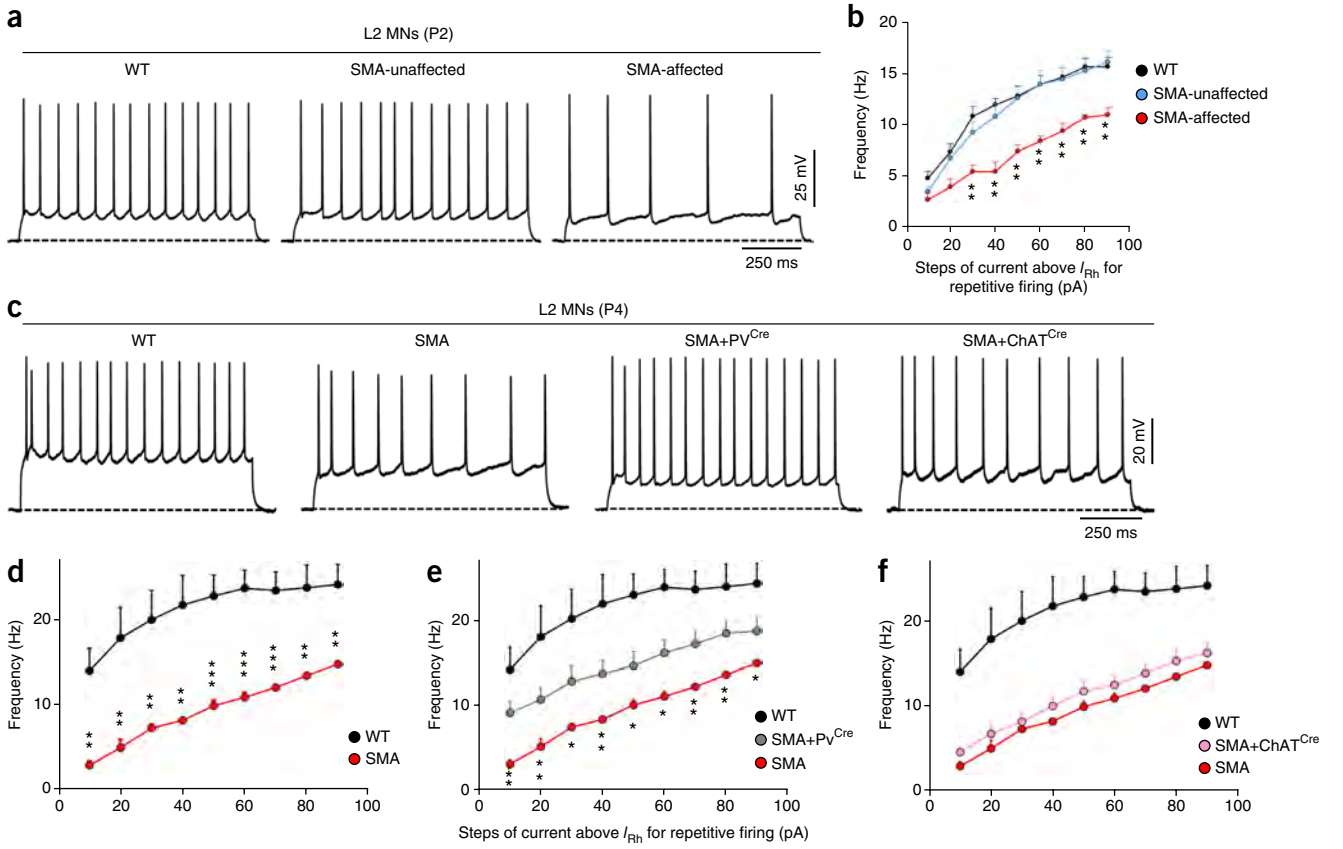

Figure 4 Improvement of reduced firing frequency in SMA MNs following selective upregulation of SMN in proprioceptive neurons only. (**a**) Intracellular responses of repetitive firing following current injection of 50 pA above the minimum current required for continuous firing for a WT ($n = 7$), SMA-unaffected ($n = 6$) and SMA-affected ($n = 4$) MN at P2. (**b**) Frequency-to-current relationship for the three groups shown in **a**. One-way ANOVA, Tukey's *post hoc* analysis, $^{**}P < 0.01$ (WT versus SMA-affected for individual steps of current). I_{Rh} is the rheobase. For details, see **Supplementary Methods Checklist**. (**c**) Intracellular responses of repetitive firing following current injection of 50 pA above the minimum current required for continuous spiking, in a WT, SMA, SMA+Pv^{Cre} and SMA+ChAT^{Cre} MN at P4. (**d**) Frequency-to-current relationship for WT and SMA MNs at P4. $^{**}P < 0.01$, $^{***}P < 0.001$, unpaired *t*-test for the individual steps of current. (**e**) Frequency-to-current relationship for WT, SMA and SMA+Pv^{Cre} MNs at P4. $^{*}P < 0.05$, $^{**}P < 0.01$, unpaired *t*-test for the individual steps of current (SMA versus SMA+Pv^{Cre}). (**f**) Frequency-to-current relationship for WT, SMA and SMA+ChAT^{Cre} MNs at P4. Not significant; $P \geq 0.14$ (SMA versus SMA+ChAT^{Cre}). All data are represented as mean ± s.e.m. For details, see **Supplementary Methods Checklist**.

Next we measured the EPSP amplitude in L2 MNs following proprioceptive fiber stimulation at P4. We did not observe any significant changes in the MN resting membrane potential for any of the experimental groups at P4 (mean ± s.e.m.; one-way ANOVA, $P = 0.539$ (*F*-test). Notably, the reduction of the EPSP amplitude in SMA MNs was restored in SMA+Pv^{Cre} but not in SMA+ChAT^{Cre} MNs (**Fig. 2c**,**d**). Furthermore, analysis of the EPSP amplitude and input resistance (**Fig. 2e**) demonstrated that MNs exhibiting large EPSPs possessed low input resistances. This relationship was similar in WT and SMA+Pv^{Cre} MNs (**Fig. 2e**). To address whether the reduction in EPSP amplitude is due to impaired glutamate release, we performed paired-pulse stimulation of the dorsal root at 1 Hz. Proprioceptive stimulus-induced EPSPs in WT mice were mildly depressed at P4, as previously reported[26]. However, EPSPs in SMA mice were significantly more depressed than those in WT (**Fig. 2f**,**g**). This depression was corrected in SMA+Pv^{Cre} mice, but not in SMA+ChAT^{Cre} mice (**Fig. 2f**,**g**). Thus, the reduction of EPSPs in SMA is due to impairment of glutamate release.

To address whether the improved EPSP amplitude in SMA+Pv^{Cre} MNs was due to a rescue of proprioceptive synapses or enhanced presynaptic function of the remaining synapses, we analyzed the number of VGluT1^{+} synapses on retrogradely filled MNs. There was a significant rescue of VGluT1 synapses both on the somata and dendrites of MNs in SMA+Pv^{Cre} mice at P4 (**Fig. 2h–j**), whereas SMA+ChAT^{Cre} MNs showed no rescue (**Fig. 2h–j**). Furthermore, we found that VGluT1 synapse numbers in SMA+Pv^{Cre} mice remained comparable to WT synaptic numbers at P11, a late stage of disease (**Supplementary Fig. 8a–c**), demonstrating that proprioceptive synapses continue to develop. Thus, restoration of SMN in proprioceptive neurons rescues synaptic loss. Collectively, our results demonstrate that MN dysfunction is a non-cell-autonomous consequence of SMN-dependent deficits in proprioceptive neurons.

Dysfunction and death of MNs are two independent events in SMA

MN death is a hallmark of SMA[10]. MN hyperexcitability has been implicated in neuronal death following axotomy of facial MNs[27] and in amyotrophic lateral sclerosis[28]. We therefore asked whether selective SMN upregulation in proprioceptive neurons would affect the survival of SMA MNs. We demarcated the L2 rostrocaudal extent as we previously described[13] and counted all L2 MNs identified by ChAT staining at P2, P4 and P11. There was no significant MN loss at P2, but 34% of MNs were lost at P4 and 42% at P11 (**Fig. 3a**,**b**). SMN restoration in proprioceptive neurons only (SMA+Pv^{Cre}) did not result in any

significant rescue (P = 0.68, SMA versus SMA+Pv^{Cre}), whereas selective restoration in MNs (SMA+ChAT^{Cre}) resulted in rescue of MNs both at P4 and at P11, which was not ameliorated any further by SMN upregulation in both proprioceptive neurons and MNs (SMA+(Pv+ChAT)^{Cre} mice) (**Fig. 3a**,**b**). These results demonstrate that SMN deficiency in sensory neurons does not induce the death of MNs. Thus, dysfunction and death of MNs are distinct and independent events, likely governed by different mechanisms.

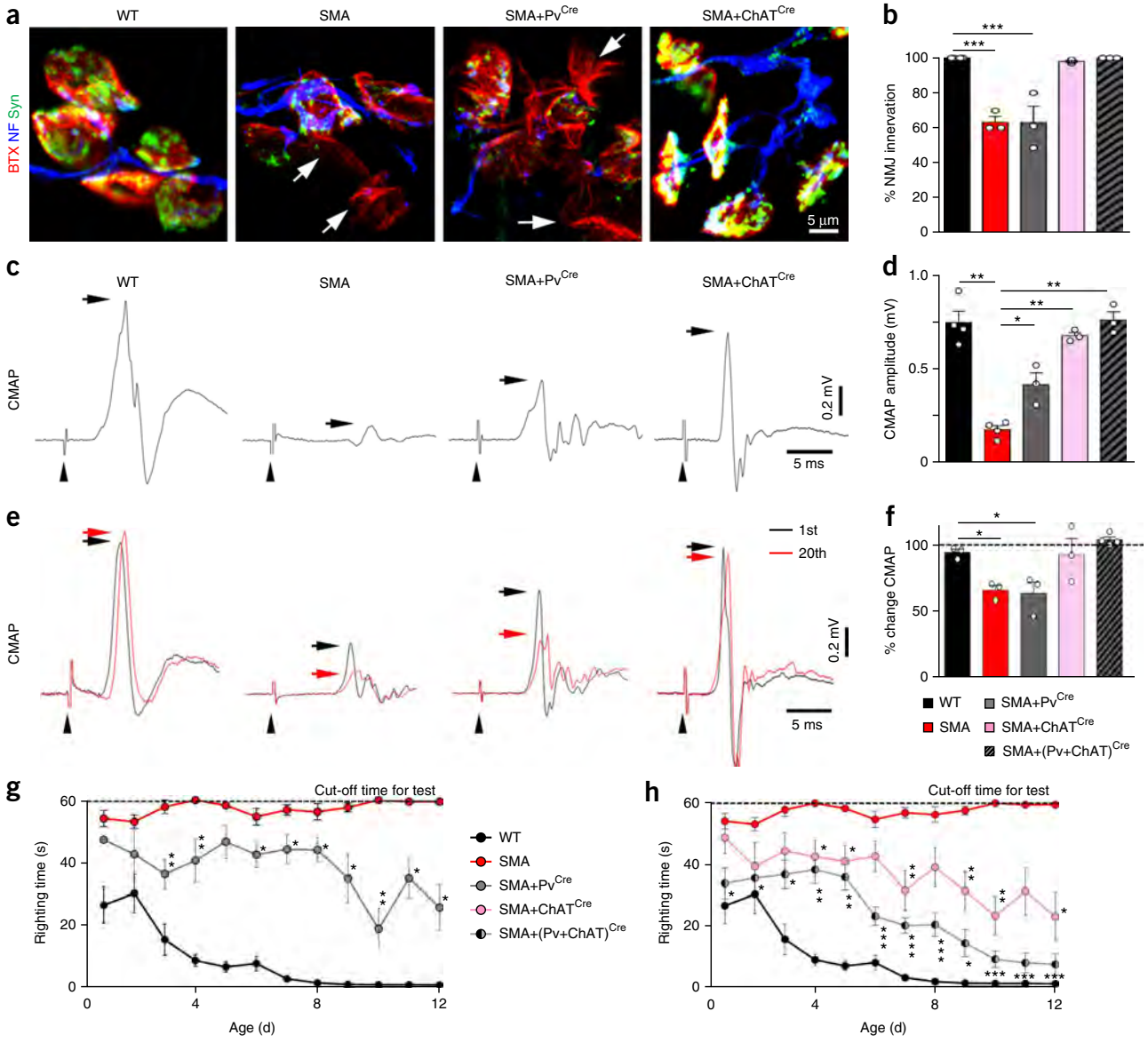

Figure 5 Improvement of NMJ function, innervation and behavioral benefits following selective restoration of SMN in proprioceptive neurons and MNs. (**a**) Confocal images of NMJs from the QL muscle labeled by the presynaptic markers synaptophysin (Syn, green) and neurofilament (NF, blue) and the postsynaptic marker bungarotoxin (BTX, red) in WT, SMA, SMA+Pv^{Cre} and SMA+ChAT^{Cre} mice at P4. Arrows indicate denervated NMJs. (**b**) Percentage extent of innervation of the QL muscle in WT (n = 4), SMA (n = 4), SMA+Pv^{Cre} (n = 3), SMA+ChAT^{Cre} (n = 3) and SMA+(Pv+ChAT)^{Cre} (n = 3). One-way ANOVA, Tukey's *post hoc* analysis, ***P < 0.001. (**c**) CMAP recorded from the QL muscle following stimulation of the L2 ventral root in WT, SMA, SMA+Pv^{Cre} and SMA+ChAT^{Cre} mice at P4. Arrows indicate the peak CMAP amplitude and arrowheads the stimulus artifact. (**d**) Average of peak CMAP amplitude for the groups shown in **c**. One-way ANOVA, Tukey's *post hoc* analysis (*P = 0.018, **P < 0.0001). (**e**) CMAP recorded from the QL muscle following 20-Hz stimulation of the L2 ventral root in WT, SMA, SMA+Pv^{Cre} and SMA+ChAT^{Cre} mice at P4. The 1st (black) and 20th (red) CMAP are shown superimposed. Horizontal arrows indicate the peak CMAP amplitude and arrowheads the stimulus artifact. (**f**) Percentage change of CMAP amplitude expressed as a ratio of the 20th to the 1st response in WT, SMA, SMA+Pv^{Cre}, SMA+ChAT^{Cre} and SMA+(Pv+ChAT)^{Cre} mice at P4. One-way ANOVA, Tukey's *post hoc* analysis (*P = 0.025, WT versus SMA and *P = 0.018, WT versus SMA+Pv^{Cre}). (**g**) Righting times for WT (black), SMA (red) and SMA mice in which SMN was restored in proprioceptive neurons only (SMA+Pv^{Cre}; gray). *P < 0.05, **P < 0.01, t-test (SMA+Pv^{Cre} versus SMA) for the individual ages. (**h**) Righting times for WT mice (black), SMA mice (red), SMA mice in which SMN was restored in MNs only (SMA+ChAT^{Cre}; pink), and SMA mice in which SMN was restored in both proprioceptive neurons and MNs (SMA+(Pv+ChAT)^{Cre}; black/gray). *P < 0.05, **P < 0.01, ***P < 0.001, unpaired t-test (SMA versus SMA+Pv^{Cre} and SMA versus SMA+(Pv+ChAT)^{Cre}). All data are represented as mean ± s.e.m. For details, see **Supplementary Methods Checklist**.

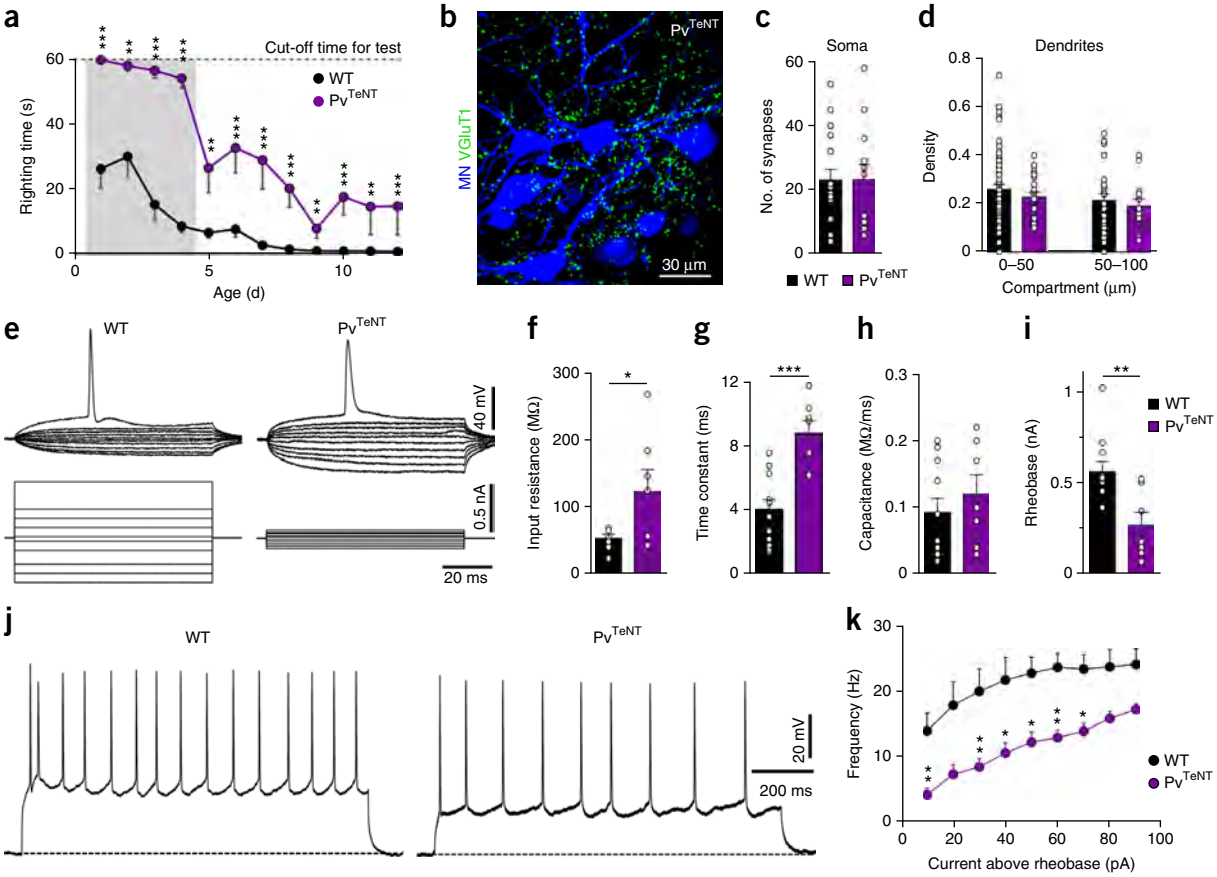

Figure 6 Neurotransmission block in proprioceptive neurons by tetanus toxin renders WT MNs dysfunctional. (**a**) Righting time for WT (black, $n = 14$) and Pv^{TeNT} (violet, $n = 8$) mice. $^{**}P < 0.01$, $^{***}P < 0.001$, unpaired *t*-test for the individual ages. Shaded area indicates the inability of in Pv^{TeNT} mice to right themselves during the first 4 postnatal days. (**b**) *z*-stack projection of confocal images from retrogradely labeled L2 MNs (blue) and VGluT1 synaptic boutons (green) in a Pv^{TeNT} mouse at P4. The total distance in the *z* axis was 7 µm (20 optical planes at 0.35-µm intervals). (**c**) The average number of VGluT1 boutons on the entire somata of L2 WT and Pv^{TeNT} MNs. (**d**) VGluT1 synaptic density on 50-µm dendritic compartments from the soma, for WT and Pv^{TeNT} mice. (**e**) Membrane responses (top) following current injection (bottom) in a WT and a Pv^{TeNT} L2 MN at P4. (**f**) The average input resistance for WT ($n = 11$) and Pv^{TeNT} ($n = 7$) MNs at P4. $^{*}P = 0.0163$, unpaired *t*-test. (**g**) The average membrane time constant for WT and Pv^{TeNT} MNs at P4. $^{***}P = 0.0003$, unpaired *t*-test. (**h**) The average capacitance for WT and Pv^{TeNT} MNs at P4. (**i**) The average rheobase current for WT and Pv^{TeNT} MNs at P4. $^{**}P = 0.0056$, unpaired *t*-test. (**j**) Intracellular responses of repetitive firing following 50 pA current injection above the minimum current required for continuous spiking, for a WT and a Pv^{TeNT} MN at P4. (**k**) Frequency-to-current relationships for WT and Pv^{TeNT} MNs at P4. $^{*}P < 0.05$, $^{**}P < 0.01$, unpaired *t*-test at individual steps of current. All data are represented as mean ± s.e.m. For details, see **Supplementary Methods Checklist**.

Dysfunction of proprioceptive synapses causes reduction in MN firing in SMA

The effects of increased input resistance on neuronal firing in neurodegenerative diseases are poorly understood. To address this, we analyzed the firing frequency in L2 MNs following current injection. The current injection required to induce repetitive firing in WT and SMA P2 MNs was variable (**Supplementary Fig. 9a–c**). Thus, we compared among the groups the MN firing frequency induced by increments of current above the minimum current required for repetitive firing. The firing frequency of SMA-unaffected MNs was indistinguishable from that of control MNs (**Fig. 4a,b**). However, SMA-affected MNs, despite exhibiting increased input resistance (**Fig. 1a–e**), paradoxically displayed reduced firing rates compared to controls at P2 (**Fig. 4a,b**). Notably, SMA-resistant L5 MNs, which did not exhibit increased input resistance, did not display any significant changes in firing frequency ($P \geq 0.57$; **Supplementary Fig. 9d,e**).

At P4, when nearly all SMA L2 MNs exhibit increased input resistance, all SMA MNs fired at significantly lower frequencies (**Fig. 4c,d**). Remarkably, SMA+Pv^{Cre} MNs exhibited a significant correction in firing frequency (**Fig. 4c,e**), whereas SMA+$ChAT^{Cre}$ MNs fired at similar frequencies to SMA MNs (**Fig. 4c,f**). Although SMA MNs exhibited a reduction in the voltage threshold compared to WT (WT: −26.6 ± 1.7 mV; SMA: −39.7 ± 2.4 mV; $P = 0.0011$, Mann–Whitney), in agreement with our previous report[13], SMA+Pv^{Cre} and SMA+$ChAT^{Cre}$ MNs had similar voltage threshold values to SMA MNs. Thus, SMA MNs fire at reduced frequencies and this reduction may be triggered by the dysfunction of sensory–motor synapses.

SMN upregulation in proprioceptive neurons in SMA mice improves NMJ function and motor behavior

We next investigated the effects of selective restoration of SMN in proprioceptive neurons at the neuromuscular junction (NMJ) by examining the functional and morphological properties of NMJs in the vulnerable QL muscles of SMA mice, at P4. We found that the QL exhibited 37% denervation in SMA mice and 38% in SMA+Pv^{Cre} mice (**Fig. 5a,b**). In contrast, we observed a complete rescue of NMJ denervation when SMN was restored in MNs only (SMA+$ChAT^{Cre}$) or in both neuronal classes [SMA+$(Pv+ChAT)^{Cre}$] (**Fig. 5a,b**). Next we

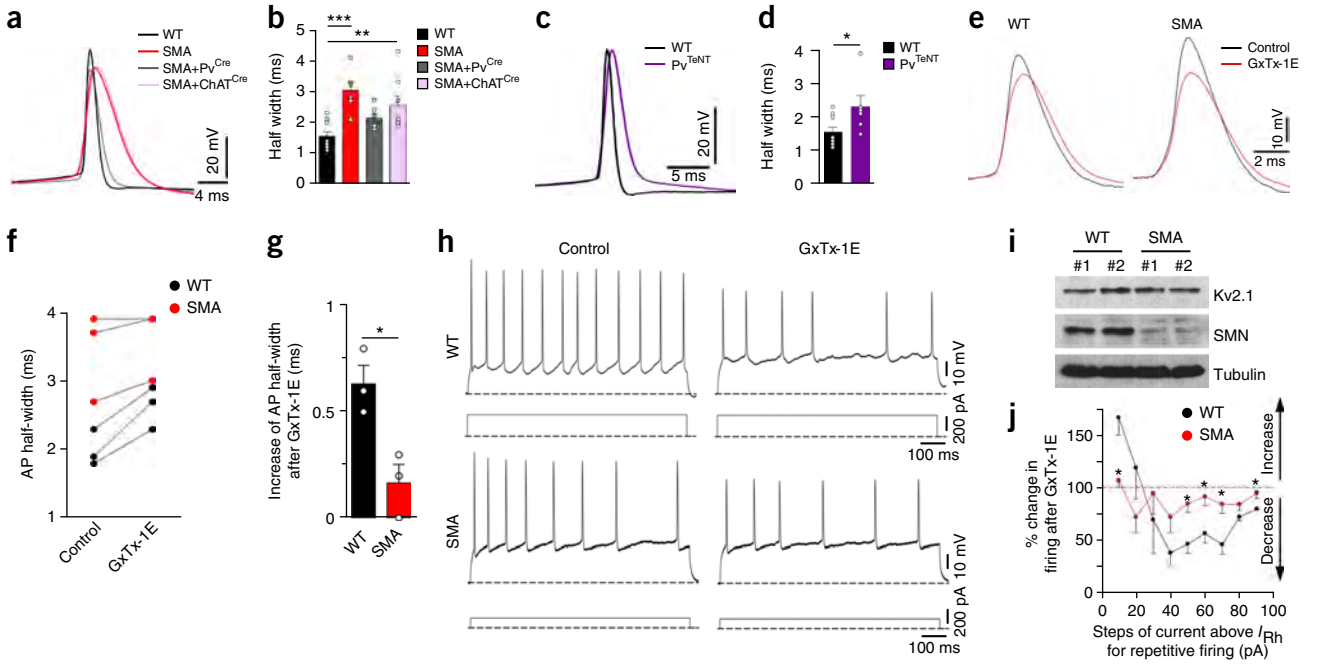

Figure 7 Prolongation of action potentials through the delayed rectifier channels is associated with reduction in firing frequency in SMA and Pv^{TeNT} MNs. (**a**) Action potentials during steady-state firing following current injection in WT (black, $n = 8$), SMA (red, $n = 6$), SMA+Pv^{Cre} (gray, $n = 6$) and SMA+$ChAT^{Cre}$ (pink, $n = 8$) L2 MNs at P4. (**b**) Average duration of action potential half-width for the groups shown in **a**. One-way ANOVA, Tukey's *post hoc* analysis (***$P < 0.001$, **$P < 0.01$). (**c**) Action potentials during steady-state firing following current injection in a WT (black, $n = 8$) and a Pv^{TeNT} (violet, $n = 6$) L2 MN at P4. (**d**) Average duration of half-width from action potentials for WT and Pv^{TeNT} MNs. *$P = 0.042$, unpaired *t*-test. (**e**) Superimposed action potentials before (black) and after (red) GxTx-1E (100 nM) exposure in a WT and an SMA MN. (**f**) Change of action potential half-width before and after GxTx-1E exposure in WT (black) and SMA (red) MNs. (**g**) Average increase in the action potential half-width following GxTx-1E exposure in WT (black) and SMA (red) MNs. *$P = 0.034$, paired *t*-test. (**h**) Intracellular responses following current injection in control solution and after GxTx-1E exposure in a WT and an SMA MN. (**i**) Western blot analysis for Kv2.1, SMN and β-tubulin protein expression from two WT and two SMA ventral spinal cords at P4. Full-length blots are available in **Supplementary Figure 16**. (**j**) Percentage change in firing frequency following GxTx-1E exposure with 10-pA steps in current injection for WT and SMA MNs. The relative increase or decrease in firing frequency is indicated on the right. *$P < 0.05$, unpaired *t*-test for the individual steps of current. All data are represented as mean ± s.e.m. For details, see **Supplementary Methods Checklist**.

developed an assay that measures NMJ function by stimulating MN axons in the L2 ventral root and recording the resultant compound muscle action potential (CMAP) in the QL muscle (**Supplementary Fig. 10a**). This assay is uncontaminated by electrical activity from motor axons, as exposure to pancuronium resulted in complete abolition of the CMAP (**Supplementary Fig. 10c**).

We found that the CMAP amplitude was significantly reduced in SMA mice (**Fig. 5c**,**d**). Strikingly, selective upregulation of SMN in SMA+Pv^{Cre} mice resulted in a significant improvement (2.3-fold increase) in CMAP amplitude, while SMA+$ChAT^{Cre}$ mice exhibited a more robust (3.8-fold increase) improvement (**Fig. 5c**,**d**). Restoration of SMN in both neuronal types resulted in recovery to WT levels (**Fig. 5c**,**d**). To assess CMAP reliability, we applied a train of stimuli at 20 Hz (**Supplementary Fig. 10b**). WT, SMA+$ChAT^{Cre}$ and SMA+$(Pv+ChAT)^{Cre}$ mice showed reliable CMAP responses (**Fig. 5e**,**f**). In contrast, SMA and SMA+Pv^{Cre} exhibited a ~35% decline by the end of the stimulus train. Thus, SMN restoration in proprioceptive neurons moderately improves NMJ function, but not denervation.

To assess the behavioral benefits of selective SMN restoration in proprioceptive neurons, MNs, or both neuronal populations, we analyzed the righting time of SMA mice. We found that SMA+Pv^{Cre} mice exhibited improved righting time as early as P3 (**Fig. 5g**) and modestly increased lifespan (**Supplementary Fig. 10d**). Furthermore, while selective restoration of SMN in MNs improved the righting time (**Fig. 5h**) and increased lifespan (**Supplementary Fig. 10e**), as previously reported[20], combinatorial SMN upregulation in both proprioceptive neurons and MNs in SMA+$(Pv+ChAT)^{Cre}$ mice yielded a synergistic improvement of motor behavior beyond that in SMA+$ChAT^{Cre}$ mice (**Fig. 5h**). These results demonstrate that SMN deficiency in proprioceptive neurons contributes to the motor deficits in SMA.

Block of neurotransmitter release from proprioceptive synapses causes MN dysfunction during early development

To tease out the synaptic mechanisms responsible for MN dysfunction, we investigated whether impaired glutamate release from proprioceptive synapses is responsible for the increased input resistance and reduced firing frequency of MNs. We blocked neurotransmission at proprioceptive synapses through expression of the tetanus toxin light chain subunit (TeNT), which inhibits neurotransmitter release[29]. A Pv^{Cre} driver mouse line was crossed to a $ROSA26^{lsl\text{-}TeNT}$ mouse strain[30] to generate Pv^{TeNT} mice. Pv^{TeNT} mice have a short lifespan, surviving on average until P18, and exhibit severe defects in motor coordination, including a nearly complete inability to right during the first 4 postnatal days (**Fig. 6a**). As we reported recently[22], these mice display nearly complete (~97%) block of neurotransmission from proprioceptive synapses on MNs. Pv^{TeNT} mice showed no loss of VGluT1 synapses from the somata and proximal dendrites of L2 MNs (**Fig. 6b–d**). However, Pv^{TeNT} L2 MNs exhibited a significantly increased input resistance and time constant and reduced rheobase (**Fig. 6e–i**). These changes were not due to a reduction in MN size,

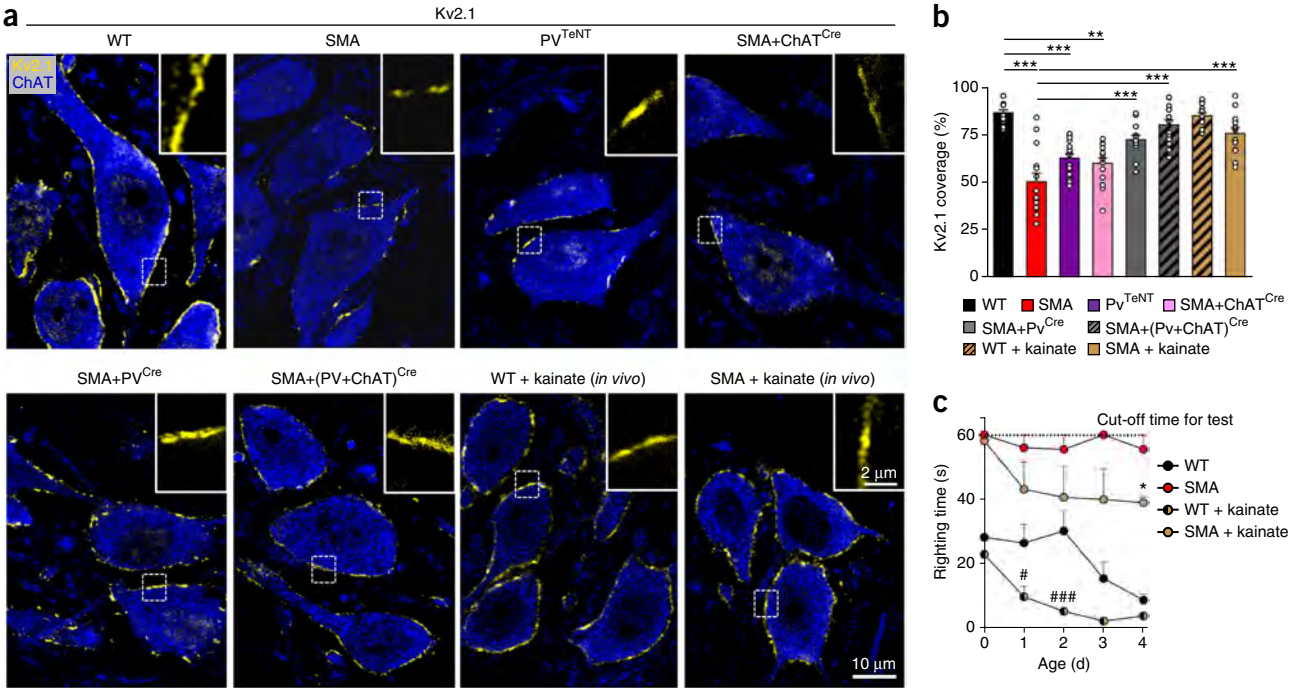

Figure 8 Loss of SMN from proprioceptors reduces the surface expression of Kv2.1 in MNs. (**a**) Single-optical-plane confocal images of P4 L2 MNs (ChAT in blue) expressing Kv2.1 channels (yellow) for WT ($n = 14$), SMA ($n = 14$), Pv^{TeNT} ($n = 15$), $SMA+ChAT^{Cre}$ ($n = 14$), $SMA+Pv^{Cre}$ ($n = 13$) and $SMA+(Pv+ChAT)^{Cre}$ ($n = 16$) mice, as well as WT ($n = 13$) and SMA mice ($n = 14$) treated *in vivo* with kainate. Insets show Kv2.1 immunoreactivity of the boxed dotted area at higher magnification. (**b**) Percentage somatic coverage of Kv2.1 expression in MNs for the same experimental groups shown in **a**. One-way ANOVA, Tukey's *post hoc* analysis ($^{**}P < 0.01$, $^{***}P < 0.001$). All data are represented as mean ± s.e.m. (**c**) Righting times following daily *in vivo* kainate treatment (1.5 mg/kg) for WT and SMA mice. $^{*}P < 0.05$, unpaired *t*-test, SMA untreated versus SMA kainate-treated mice. $^{\#}P < 0.05$ and $^{\#\#\#}P < 0.001$, unpaired *t*-test, WT untreated versus WT kainate-treated mice. For details, see **Supplementary Methods Checklist**.

since the capacitance did not change (**Fig. 6h**). L5 Pv^{TeNT} MNs also increased their input resistance (**Supplementary Fig. 11f–h**), suggesting that glutamatergic block from proprioceptive synapses causes input resistance changes in all MNs and is not specific to certain MN pools. Furthermore, frequency–current plots from L2 Pv^{TeNT} MNs at P4 revealed a significant reduction in firing frequency (**Fig. 6j,k**), indicating that neurotransmission block at sensory–motor synapses affects MN firing frequency. There was no significant loss of L2 MNs ($P = 0.39$; **Supplementary Fig. 11a**), NMJ denervation in the QL muscle (**Supplementary Fig. 11b,c**) or significant changes in CMAP amplitude ($P = 0.23$; **Supplementary Fig. 11d,e**).

To test the possibility that signaling from brain-derived neurotrophic factor (BDNF)—known to be released by proprioceptive neurons[31,32]—may also be responsible for MN dysfunction, we overexpressed BDNF in SMA mice by transducing proprioceptive neurons with an AAV9-GFP-mBDNF adeno-associated virus pseudotype 9, injected intracerebroventricularly at birth, and examined the function of SMA MNs at P5 (see Online Methods and **Supplementary Fig. 12**). Approximately 85% of proprioceptive neurons and 50% of MNs were transduced (**Supplementary Fig. 12a–d**). BDNF release from SMA proprioceptive synapses was confirmed by an increase of GAD65—but not GAD67—in GABApre (inhibitory neurons responsible for presynaptic inhibition) synapses (**Supplementary Fig. 12e–h**), as we reported for $VGluT1^{-/-}$ ($Slc17a7^{-/-}$) mice[32]. To avoid the effects of direct BDNF overexpression in SMA MNs, we analyzed untransduced SMA MNs only (**Supplementary Fig. 12i**). Thus, any possible changes would be due to overexpression of BDNF in proprioceptive neurons. We found that untransduced SMA MNs exhibited similar increases in input resistance and reduced firing frequency compared to control MNs from SMA mice that did not receive AAV9-BDNF (**Supplementary Fig. 12i–l**). Taken together, these results suggest that changes in SMA MN function are unlikely to be mediated by BDNF release from proprioceptive neurons.

Collectively, these results demonstrate that block of glutamate release at sensory–motor synapses results in increased MN input resistance and a concomitant reduction in firing frequency, but not MN death, phenocopying aspects of SMA . Thus, presynaptic function impairment is likely to be responsible for MN dysfunction in SMA.

Sensory–motor synaptic dysfunction in SMA leads to a widening of the MN spike waveform

We sought to decipher the molecular mechanisms of MN dysfunction, causally linking the reduction in firing frequency with decreased sensory–motor excitatory synaptic drive, by comparing the orthodromically induced action potential profiles of SMA and WT MNs during steady-state repetitive firing induced by current injection. The afterhyperpolarization (AHP) is unlikely to contribute to the reduction in spiking frequency in SMA MNs, because there was no significant difference in either AHP amplitude or duration ($P = 0.20$; **Supplementary Fig. 13a,b**). Examination of the action potential duration revealed significantly prolonged action potentials in SMA MNs compared to WT controls as illustrated by the increase of the action potential half-width (**Fig. 7a,b**). Notably, $SMA+Pv^{Cre}$ MNs exhibited action potentials similar to those observed in WT, while action potentials in $SMA+ChAT^{Cre}$ MNs were similar to those in SMA MNs (**Fig. 7a,b**). Furthermore, Pv^{TeNT} MNs exhibited prolonged action

potentials akin to those in SMA MNs (**Fig. 7c**,**d**). Although the rate of depolarization in action potentials was similar among the four experimental groups (WT: 36.7 ± 3.1; SMA: 34.8 ± 4.0; SMA+Pv^{Cre}: 29.4 ± 1.2; SMA+ChAT^{Cre}: 33.8 ± 6.6 mV/ms (one-way ANOVA, $P = 0.649$ (F-test)), the rate of repolarization was significantly slower in SMA and SMA+ChAT^{Cre} MNs and it was corrected in SMA+Pv^{Cre} MNs (WT: 18.9 ± 2.0; SMA: 10.5 ± 1.1; SMA+Pv^{Cre}: 14.3 ± 0.9; SMA+ChAT^{Cre}: 9.4 ± 1.7 mV/ms; $P = 0.004$ in WT versus SMA and $P = 0.002$ in WT versus SMA+ChAT^{Cre}, one-way ANOVA, Tukey's *post hoc* test). Thus, widening of the spike waveform is likely responsible for the reduced output seen in SMA MNs.

Loss of SMN from proprioceptors reduces the surface expression of Kv2.1 in MNs

The slower repolarization of the action potential raised the possibility that changes in potassium channels may be responsible for spiking frequency reduction. The delayed rectifier Kv2.1 channel plays an important role in action potential repolarization in MNs[33]. We therefore investigated the contribution of Kv2.1 channels to SMA MN dysfunction. We compared the half-width of action potentials and MN firing frequency following acute exposure to a specific blocker of Kv2 channels, guangxitoxin-1E (GxTx-1E)[34,35]. GxTx-1E specifically blocks Kv2.1 and Kv2.2 at 100 nM and Kv4.3 at higher concentrations[34]. Exposure to 100 nM GxTx-1E did not alter the input resistance of WT and SMA MNs (**Supplementary Fig. 13c–e**). The action potential half-width was significantly increased in WT but only marginally increased in SMA MNs (**Fig. 7e–g**). Notably, the firing frequency following current injection was significantly reduced in WT MNs, and less affected in SMA MNs (**Fig. 7h–j**). An insight into how the reduction in Kv2 current reduces the firing ability is revealed by measurements of the trough voltage, defined as the most negative potential between two spikes during repetitive firing (**Supplementary Fig. 13f**). We found a significant increase in the trough voltage, with a shift to more depolarized potentials, in SMA MNs compared to WT when the firing frequency doubled ($P = 0.002$; **Supplementary Fig. 13g**). This depolarization may result in a reduced recovery of voltage-gated sodium channels from inactivation, ultimately limiting sodium channel availability for the initiation of subsequent spikes and thereby reducing firing frequency. Collectively, these results indicate that the reduction in spiking frequency in SMA MNs is likely to be due to a reduction in Kv2 potassium channels.

To focus on channel expression in MNs, we performed immunohistochemistry with antibodies against Kv2.1, Kv2.2 and Kv4.3. Kv2.1 in MNs was associated with proprioceptive synapses (**Supplementary Fig. 14a**). Analysis of Kv2.1 surface coverage on L2 MN somata (**Supplementary Fig. 14b**,**c**) revealed a significant reduction of Kv2.1 in SMA (**Fig. 8a**,**b**). Moreover, western blot analysis revealed no appreciable difference in the overall expression of Kv2.1 in L1–L3 ventral horns from WT and SMA mice (**Fig. 7i**), indicative of a specific reduction in MNs. The effects are specific to Kv2.1, since Kv2.2 coverage was similar in WT and SMA MNs (**Supplementary Fig. 14f**) and Kv4.3 was not expressed in MNs at this age (**Supplementary Fig. 14g**). L5 SMA-resistant MNs, which do not exhibit any reduction in firing frequency, did not display changes in Kv2.1 coverage (**Supplementary Fig. 14d**,**e**). In addition, Pv^{TeNT} and SMA+ChAT^{Cre} L2 MNs exhibited a similar reduction to SMA MNs in Kv2.1 somatic coverage (**Fig. 8a**,**b**). Similarly, L5 MNs in Pv^{TeNT} mice exhibited a significant reduction in Kv2.1 expression ($P < 0.0001$; **Supplementary Fig. 14d**,**e**). In striking contrast, SMA+Pv^{Cre} and SMA+(Pv+ChAT)^{Cre} MNs displayed a robust restoration of Kv2.1 coverage to normal levels (**Fig. 8a**,**b**). These results demonstrate that reduction of Kv2.1 expression in SMA MNs is a non-cell-autonomous consequence of proprioceptive neuron dysfunction.

Chronic postnatal kainate treatment restores normal Kv2.1 surface expression and improves motor function in SMA mice

To test the possibility that Kv2.1 coverage is regulated by excitatory synaptic transmission, we treated SMA mice daily *in vivo* (starting at P0) with kainate, a glutamate receptor agonist. Although kainate has been widely used to induce seizures[36], subconvulsive daily doses of 1.5 mg/kg were tolerated for the first postnatal week. Kainate treatment has been shown to increase neuronal activity[36]. Remarkably, P4 SMA MNs treated with kainate displayed a significant increase in Kv2.1 coverage (**Fig. 8a**,**b**), whereas kainate-treated WT MNs did not show any difference in Kv2.1 surface coverage compared to untreated controls (**Fig. 8a**,**b**). Additionally, the righting times of SMA mice treated with kainate significantly improved (**Fig. 8c**). Thus, an increase in global neuronal activity restores Kv2.1 channel expression and improves motor function in SMA mice.

DISCUSSION

Our study reveals non-cell-autonomous mechanisms that shape MN output during development and identifies a functional cascade of synaptic deficits that likely underlie muscle paralysis in SMA. We show that SMN deficiency causes sensory-derived dysfunction via the reduction of presynaptic glutamate transmission onto MNs, resulting in two opposing effects on their excitability. SMA MNs increase their input resistance but, paradoxically, reduce their firing ability. This reduction in MN spiking ability is a non-cell-autonomous consequence of the decrease in excitatory synaptic drive from proprioceptive neurons, most likely due to the reduction of Kv2.1 channel expression in MNs. Selective restoration of SMN in proprioceptive neurons reverses the changes in the membrane properties and spiking frequency of SMA MNs. Accordingly, selective blockade of sensory–motor neurotransmission in the presence of normal SMN levels phenocopied the effects of synaptic dysfunction in SMA. Kainate treatment *in vivo* restored normal Kv2.1 expression and improved motor function, presumably by increasing the excitatory drive onto MNs, and may represent a viable therapeutic approach complementary to SMN upregulation (**Supplementary Fig. 15**).

Non-cell-autonomous mechanisms of SMA MN dysfunction

Neuronal dysfunction is often determined by changes in physiological properties of disease-vulnerable neurons[13,37]. Intrinsic membrane properties determine neuronal excitability and govern how converging premotor synaptic drive is translated into the generation of action potentials[38].

We demonstrate that MN increased input resistance is a non-cell-autonomous response induced by SMN deficiency, ensuing after birth and progressively accumulating in vulnerable SMA MNs, which paradoxically impairs their functional output. First, vulnerable but not resistant SMA MNs exhibit signs of increased input resistance. Second, specific restoration of SMN in MNs does not correct their neuronal membrane properties, whereas restoration of SMN in proprioceptive neurons restores the MN input resistance to normal levels. Lastly, neurotransmission block at proprioceptive synapses (Pv^{TeNT}) phenocopies the changes in the MN membrane properties observed in SMA. Increased input resistance in vulnerable SMA MNs correlates with lower proprioceptive stimulus-induced EPSP amplitude, both of which are normalized following restoration of SMN in proprioceptive neurons. Thus, SMN deficiency in proprioceptive neurons decreases synaptic release and ultimately precipitates secondary changes in MNs.

Synaptic dysfunction may be caused by compromised presynaptic neurotransmitter release, a loss of synaptic boutons, or both. Early in SMA, the asymmetric reduction in EPSP amplitude (87%) compared to synaptic loss (49%) and the reduction in the paired-pulse stimulation study suggest that the impairment of glutamate release from sensory–motor synapses is the initiating event in SMA. Dysfunction at later stages is further exacerbated by the progressive loss of synapses from dendrites, which comprise ~90% of the total number of synapses[18] and are largely responsible for MN activation[39].

Increase in input resistance does not cause cell death

Common events in neurodegenerative diseases are death and dysfunction of vulnerable neurons. Deciphering the mechanisms responsible for these events is key in determining their contributions to the disease process. Increases in the input resistance of MNs are thought to be linked to neuronal death, as axotomy of developing MN axons causes substantial cell death[27], with subpopulations of MNs exhibiting abnormal increases in input resistance considered to represent a 'pre-lethal' stage[27]. Changes in MN excitability are also associated with neuronal death in amyotrophic lateral sclerosis[28,40]. However, a cause–effect relationship between increases in input resistance and death of MNs has not been established. Here we provide direct evidence that an increase in input resistance and death of MNs are independent, causally unrelated events induced by SMN deficiency in motor circuits. First, restoration of SMN in proprioceptive neurons restores the functional changes in MNs without rescuing the number of SMA MNs. Second, restoration of SMN in MNs rescues cell death, consistent with previous studies[20,41], but does not correct the changes in input resistance. Finally, neurotransmission block by Pv^{TeNT} increases the MN input resistance, but does not cause MN death. Thus, our work reveals that an abnormal increase in input resistance is not a trigger of MN death.

Impairment of glutamate transmission causes decline in MN output through reduction of Kv2.1 channels

What is the functional relationship between the intrinsic membrane properties and MN output? Changes in firing frequency can be governed by the AHP[42] and persistent inward currents (PICs)[38]. However, the reduction of spike firing in SMA is not due to changes in AHP because SMA MNs showed no abnormalities. Similarly, PICs are unlikely to contribute appreciably since PICs are cell-autonomously increased in SMA MNs[41]. An increase in PICs would be expected to increase the MN firing frequency, but our results in SMA+$ChAT^{Cre}$ mice demonstrated that SMN restoration in MNs did not increase their firing frequency compared to controls. However, GxTx-1E caused a ~10% global reduction in the peak of the action potential and presumably sodium currents, suggesting that PICs may modestly contribute to MN firing.

Spikes evoked at steady-state firing in SMA MNs were broader and were mostly modulated by the potassium channel Kv2.1. SMA MNs decrease their firing frequency because of a reduction in Kv2.1-mediated repolarizing currents, first leading to longer action potentials and subsequently to sustained depolarized voltages between spikes. Extended depolarization would maintain voltage-gated sodium channels in their inactivated state and decrease their availability for action potential generation. Kv2.1 channels are expressed in neurons[43], including adult MNs[44,45], and are associated with excitatory synapses including proprioceptive inputs[44], as we observed in neonatal MNs. The reduction of Kv2.1 expression in SMA MNs is due to a reduction in glutamate release from proprioceptive synapses rather than their loss, since Kv2.1 was reduced in Pv^{TeNT} animals without synaptic loss. The precise mechanisms for the reduction of Kv2.1 channels are unknown but may include impairments in gene transcription, translation or protein trafficking. Our results identify glutamate release from proprioceptive synapses as a key trigger and the reduction of Kv2.1 surface expression as the most plausible effector of changes in firing ability of SMA MNs.

Is the increased input resistance and reduction in firing of SMA MNs an adaptive or maladaptive homeostatic response to synaptic dysfunction? Kv2.1 has been described as a target for mechanisms of homeostatic plasticity[46]. Peripheral axotomy in adult MNs results in Kv2.1 reduction[45]. Since Kv2.1 channels gradually recover after axotomy, it is thought that changes in Kv2.1 expression are a homeostatic response to altered activity[45]. Here we show that vulnerable SMA MNs, which develop under chronically reduced glutamate release, exhibit a reduction in firing, suggesting that SMA MN dysfunction is a manifestation of an experience-dependent maladaptive response.

Clinical significance for MN disease

Decoding the mechanisms regulating the recruitment of MNs is critical for understanding disease mechanisms. The muscle force produced by a single motor unit is partly determined by muscle fiber number and the frequency at which these fibers are activated by the MN. In humans, the rate at which action potentials activate muscle fibers—known as rate coding—varies considerably, with low frequencies resulting in single twitches and higher frequencies producing fused tetanic contraction[47,48]. Mice also generate muscle force partly through the rate modulation of motor units[49]. Hence, the firing rate of each motor unit increases with increasing muscular effort until the maximum rate is reached[50]. Since smaller muscles recruit their motor units within 0 to 50% of maximum voluntary contraction (MVC), they rely exclusively on firing rate increase to augment their force output between 50 and 100% MVC[47]. Larger muscles recruit human motor units at least to 90% MVC[47]. Thus, smaller muscles rely primarily on firing rate and larger muscles on recruitment order to modulate their force. Here, we show that vulnerable SMA mouse MNs and MNs in Pv^{TeNT} cannot fire at high frequencies suggesting that the reduced spiking ability greatly contributes to impairment of normal muscle contractions.

In summary, our study demonstrates that a reduction of glutamatergically mediated neurotransmission from proprioceptive synapses in SMA is a major determinant in shaping MN output. Furthermore, our observations suggest that in SMA patients, although motor units may be recruited more easily, resulting in weak twitches of affected muscles, their activation would not reach fused tetanic contractions, likely leading to total muscle paralysis as the disease progresses. Therapeutically, our experiments with *in vivo* kainate treatment suggest that an increase in gross synaptic activity could alleviate the severe neurological deficits observed in SMA.

METHODS

Methods, including statements of data availability and any associated accession codes and references, are available in the online version of the paper.

Note: Any Supplementary Information and Source Data files are available in the online version of the paper.

ACKNOWLEDGMENTS

We thank M. Goulding (Salk Institute) for generously providing the R26floxstop-TeNT mice. We also thank S. Morton and T. Jessell (Columbia University) for help with VGluT1 antibody production and a kind gift of GAD65 and GAD67 antibodies. We would like to thank C. Kellendonk (Columbia University) for his kind gift of the custom-made Cre antibody. We are also grateful to J. Trimmer

(University of California, Davis) for his kind gift of Kv2.1 knockout mouse spinal cord tissue. We would like to thank T. Jessell, L. Pellizzoni, F.J. Alvarez, S. Przedborski, D. Logothetis, S. Schorge and F. Polleux for critical comments on the manuscript. G.Z.M. was supported by the NINDS, NIH (RO1-NS078375, R21-NS079981, R21-NS084185), the Department of Defense (GR.10235006), The SMA Foundation, Cure SMA, SMA-Europe and Target-ALS.

AUTHOR CONTRIBUTIONS

G.Z.M. conceived the project. E.V.F. and G.Z.M. designed the experiments. E.V.F. performed all intracellular experiments and data analysis. E.V.F., J.G.P., C.M.S., A.V. and E.D. performed immunohistochemical experiments, MN retrograde labeling, synaptic analysis, NMJ analysis and MN counts. E.V.F., C.M.S., E.D. and J.G.P. performed behavioral analysis. C.M.S. performed western blot experiments. E.V.F., J.G.P., J.I.C., E.D. and G.Z.M. performed *in vivo* experiments. X.W. and J.G.P. performed genotyping and assisted in synaptic analysis. G.Z.M. performed NMJ functional studies. G.Z.M. wrote the manuscript with input from all authors.

COMPETING FINANCIAL INTERESTS

The authors declare no competing financial interests.

1. Jessell, T.M. Neuronal specification in the spinal cord: inductive signals and transcriptional codes. *Nat. Rev. Genet.* **1**, 20–29 (2000).
2. Bleckert, A. & Wong, R.O. Identifying roles for neurotransmission in circuit assembly: insights gained from multiple model systems and experimental approaches. *Bioessays* **33**, 61–72 (2011).
3. Chen, H.H., Hippenmeyer, S., Arber, S. & Frank, E. Development of the monosynaptic stretch reflex circuit. *Curr. Opin. Neurobiol.* **13**, 96–102 (2003).
4. Garcia-Campmany, L., Stam, F.J. & Goulding, M. From circuits to behaviour: motor networks in vertebrates. *Curr. Opin. Neurobiol.* **20**, 116–125 (2010).
5. Glover, J.C. Development of specific connectivity between premotor neurons and motoneurons in the brain stem and spinal cord. *Physiol. Rev.* **80**, 615–647 (2000).
6. Rademakers, R., Neumann, M. & Mackenzie, I.R. Advances in understanding the molecular basis of frontotemporal dementia. *Nat. Rev. Neurol.* **8**, 423–434 (2012).
7. Palop, J.J. & Mucke, L. Amyloid-beta-induced neuronal dysfunction in Alzheimer's disease: from synapses toward neural networks. *Nat. Neurosci.* **13**, 812–818 (2010).
8. Montes, J., Gordon, A.M., Pandya, S., De Vivo, D.C. & Kaufmann, P. Clinical outcome measures in spinal muscular atrophy. *J. Child Neurol.* **24**, 968–978 (2009).
9. Lefebvre, S. *et al.* Identification and characterization of a spinal muscular atrophy-determining gene. *Cell* **80**, 155–165 (1995).
10. Tisdale, S. & Pellizzoni, L. Disease mechanisms and therapeutic approaches in spinal muscular atrophy. *J. Neurosci.* **35**, 8691–8700 (2015).
11. Gavrilina, T.O. *et al.* Neuronal SMN expression corrects spinal muscular atrophy in severe SMA mice while muscle-specific SMN expression has no phenotypic effect. *Hum. Mol. Genet.* **17**, 1063–1075 (2008).
12. Lotti, F. *et al.* An SMN-dependent U12 splicing event essential for motor circuit function. *Cell* **151**, 440–454 (2012).
13. Mentis, G.Z. *et al.* Early functional impairment of sensory-motor connectivity in a mouse model of spinal muscular atrophy. *Neuron* **69**, 453–467 (2011).
14. Ling, K.K., Gibbs, R.M., Feng, Z. & Ko, C.P. Severe neuromuscular denervation of clinically relevant muscles in a mouse model of spinal muscular atrophy. *Hum. Mol. Genet.* **21**, 185–195 (2012).
15. Zwambag, D.P., Ricketts, T.A. & Brown, S.H. Sarcomere length organization as a design for cooperative function amongst all lumbar spine muscles. *J. Biomech.* **47**, 3087–3093 (2014).
16. Bácskai, T., Rusznák, Z., Paxinos, G. & Watson, C. Musculotopic organization of the motor neurons supplying the mouse hindlimb muscles: a quantitative study using Fluoro-Gold retrograde tracing. *Brain Struct. Funct.* **219**, 303–321 (2014).
17. Alvarez, F.J., Villalba, R.M., Zerda, R. & Schneider, S.P. Vesicular glutamate transporters in the spinal cord, with special reference to sensory primary afferent synapses. *J. Comp. Neurol.* **472**, 257–280 (2004).
18. Rotterman, T.M., Nardelli, P., Cope, T.C. & Alvarez, F.J. Normal distribution of VGLUT1 synapses on spinal motoneuron dendrites and their reorganization after nerve injury. *J. Neurosci.* **34**, 3475–3492 (2014).
19. Lutz, C.M. *et al.* Postsymptomatic restoration of SMN rescues the disease phenotype in a mouse model of severe spinal muscular atrophy. *J. Clin. Invest.* **121**, 3029–3041 (2011).
20. Martinez, T.L. *et al.* Survival motor neuron protein in motor neurons determines synaptic integrity in spinal muscular atrophy. *J. Neurosci.* **32**, 8703–8715 (2012).
21. McGovern, V.L. *et al.* SMN expression is required in motor neurons to rescue electrophysiological deficits in the SMNΔ7 mouse model of SMA. *Hum. Mol. Genet.* **24**, 5524–5541 (2015).
22. Mendelsohn, A.I., Simon, C.M., Abbott, L.F., Mentis, G.Z. & Jessell, T.M. Activity regulates the incidence of heteronymous sensory-motor connections. *Neuron* **87**, 111–123 (2015).
23. Altman, J. & Bayer, S.A. *Development of the Cerebellar System* (CRC, New York, 1997).
24. Hesse, B., Fischer, M.S. & Schilling, N. Distribution pattern of muscle fiber types in the perivertebral musculature of two different sized species of mice. *Anat. Rec. (Hoboken)* **293**, 446–463 (2010).
25. Liu, Q. & Dreyfuss, G. A novel nuclear structure containing the survival of motor neurons protein. *EMBO J.* **15**, 3555–3565 (1996).
26. Li, Y. & Burke, R.E. Short-term synaptic depression in the neonatal mouse spinal cord: effects of calcium and temperature. *J. Neurophysiol.* **85**, 2047–2062 (2001).
27. Umemiya, M., Araki, I. & Kuno, M. Electrophysiological properties of axotomized facial motoneurones that are destined to die in neonatal rats. *J. Physiol. (Lond.)* **462**, 661–678 (1993).
28. Wainger, B.J. *et al.* Intrinsic membrane hyperexcitability of amyotrophic lateral sclerosis patient-derived motor neurons. *Cell Rep.* **7**, 1–11 (2014).
29. Humeau, Y., Doussau, F., Grant, N.J. & Poulain, B. How botulinum and tetanus neurotoxins block neurotransmitter release. *Biochimie* **82**, 427–446 (2000).
30. Zhang, Y. *et al.* V3 spinal neurons establish a robust and balanced locomotor rhythm during walking. *Neuron* **60**, 84–96 (2008).
31. Betley, J.N. *et al.* Stringent specificity in the construction of a GABAergic presynaptic inhibitory circuit. *Cell* **139**, 161–174 (2009).
32. Mende, M. *et al.* Sensory-derived glutamate regulates presynaptic inhibitory terminals in mouse spinal cord. *Neuron* **90**, 1189–1202 (2016).
33. Gao, B.X. & Ziskind-Conhaim, L. Development of ionic currents underlying changes in action potential waveforms in rat spinal motoneurons. *J. Neurophysiol.* **80**, 3047–3061 (1998).
34. Herrington, J. *et al.* Blockers of the delayed-rectifier potassium current in pancreatic beta-cells enhance glucose-dependent insulin secretion. *Diabetes* **55**, 1034–1042 (2006).
35. Liu, P.W. & Bean, B.P. Kv2 channel regulation of action potential repolarization and firing patterns in superior cervical ganglion neurons and hippocampal CA1 pyramidal neurons. *J. Neurosci.* **34**, 4991–5002 (2014).
36. Lee, J.K. *et al.* Decursin attenuates kainic acid-induced seizures in mice. *Neuroreport* **25**, 1243–1249 (2014).
37. Kuo, J.J. *et al.* Hyperexcitability of cultured spinal motoneurons from presymptomatic ALS mice. *J. Neurophysiol.* **91**, 571–575 (2004).
38. Powers, R.K. & Binder, M.D. Input-output functions of mammalian motoneurons. *Rev. Physiol. Biochem. Pharmacol.* **143**, 137–263 (2001).
39. Redman, S. Junctional mechanisms at group Ia synapses. *Prog. Neurobiol.* **12**, 33–83 (1979).
40. Devlin, A.C. *et al.* Human iPSC-derived motoneurons harbouring TARDBP or C9ORF72 ALS mutations are dysfunctional despite maintaining viability. *Nat. Commun.* **6**, 5999 (2015).
41. Gogliotti, R.G. *et al.* Motor neuron rescue in spinal muscular atrophy mice demonstrates that sensory-motor defects are a consequence, not a cause, of motor neuron dysfunction. *J. Neurosci.* **32**, 3818–3829 (2012).
42. Kernell, D. The limits of firing frequency in cat lumbosacral motoneurones possessing different time course of afterhyperpolarization. *Acta Physiol. Scand.* **65**, 87–100 (1965).
43. Scannevin, R.H., Murakoshi, H., Rhodes, K.J. & Trimmer, J.S. Identification of a cytoplasmic domain important in the polarized expression and clustering of the Kv2.1 K+ channel. *J. Cell Biol.* **135**, 1619–1632 (1996).
44. Muennich, E.A. & Fyffe, R.E. Focal aggregation of voltage-gated, Kv2.1 subunit-containing, potassium channels at synaptic sites in rat spinal motoneurones. *J. Physiol. (Lond.)* **554**, 673–685 (2004).
45. Romer, S.H. *et al.* Redistribution of Kv2.1 ion channels on spinal motoneurons following peripheral nerve injury. *Brain Res.* **1547**, 1–15 (2014).
46. Misonou, H. *et al.* Regulation of ion channel localization and phosphorylation by neuronal activity. *Nat. Neurosci.* **7**, 711–718 (2004).
47. De Luca, C.J., LeFever, R.S., McCue, M.P. & Xenakis, A.P. Behaviour of human motor units in different muscles during linearly varying contractions. *J. Physiol. (Lond.)* **329**, 113–128 (1982).
48. Thomas, C.K. Human motor units studied by spike-triggered averaging and intraneural motor axon stimulation. *Adv. Exp. Med. Biol.* **384**, 147–160 (1995).
49. Ritter, L.K., Tresch, M.C., Heckman, C.J., Manuel, M. & Tysseling, V.M. Characterization of motor units in behaving adult mice shows a wide primary range. *J. Neurophysiol.* **112**, 543–551 (2014).
50. De Luca, C.J. Control properties of motor units. *J. Exp. Biol.* **115**, 125–136 (1985).

ONLINE METHODS

Animals. All surgical procedures were performed on postnatal mice in accordance with the National Institutes of Health Guidelines on the Care and Use of Animals and approved by the Columbia Animal Care and Use Committee (IACUC). Animals of both sexes were used in this study.

The original breeding pairs for the SMA mice used in our study (*Smn*$^{+/-}$;*SMN2*$^{+/+}$;*SMNΔ7*$^{+/+}$) were purchased from Jackson Laboratory (Jax stock #005025; FVB background), as were PV^{Cre} (Jax stock #008069) and ChAT^{Cre} (Jax stock #006410) mice. Pv^{Cre} and ChAT^{Cre} mice (C57Bl6 background) were bred to generate *Pv*$^{Cre+/-}$;*Smn*$^{+/-}$;*SMN2*$^{+/+}$;*SMNΔ7*$^{+/+}$, *Chat*$^{Cre+/-}$;*Smn*$^{+/-}$;*SMN2*$^{+/+}$;*SMNΔ7*$^{+/+}$ and *Pv*$^{Cre+/-}$;*Chat*$^{Cre+/-}$;*Smn*$^{+/-}$;*SMN2*$^{+/+}$;*SMNΔ7*$^{+/+}$ mice. These strains were bred with SMA mice expressing a *Smn* Cre-inducible allele[19] (*Smn*^{Res}; Jax stock #007951). Cre^{-} SMA mice were null for the *Smn* allele, Cre-absent and carrying the *Smn*^{Res} allele (*Smn*$^{Res/-}$;*SMN2*$^{+/+}$;*SMNΔ7*$^{+/+}$). Cre^{+} SMA animals carried one allele of the *Smn*^{Res}, lacked endogenous mouse *Smn* and were heterozygous for either or both of Pv^{Cre} and ChAT^{Cre} (*Pv*$^{Cre+/-}$;*Smn*$^{Res/-}$;*SMN2*$^{+/+}$;*SMNΔ7*$^{+/+}$, *Chat*$^{Cre+/-}$;*Smn*$^{Res/-}$;*SMN2*$^{+/+}$;*SMNΔ7*$^{+/+}$ and *Pv*$^{Cre+/-}$;*Chat*$^{Cre+/-}$;*Smn*$^{Res/-}$;*SMN2*$^{+/+}$;*SMNΔ7*$^{+/+}$). WT mice were homozygous for *Smn* and in the absence of Cre (*Smn*$^{+/+}$;*SMN2*$^{+/+}$;*SMNΔ7*$^{+/+}$). Pv^{Cre} (ref. 51) and R26$^{floxstop\text{-}TeNT}$ (ref. 30) have been described. R26$^{floxstop\text{-}TeNT}$ mice were provided by M. Goulding (Salk Institute) and bred with Pv^{Cre} mice to obtain Pv^{TeNT} mice, as published recently[22].

Genotyping. Tail DNA PCR genotyping protocols for *SMA-Δ7* mice were followed as described on the Jackson website (for mouse *Smn*, https://www2.jax.org/protocolsdb/f?p=116:5:0::NO:5:P5_MASTER_PROTOCOL_ID,P5_JRS_CODE:11310,005025; for *SMN2*, https://www2.jax.org/protocolsdb/f?p=116:5:0::NO:5:P5_MASTER_PROTOCOL_ID,P5_JRS_CODE:1644,005025). Genotyping for the *R26*$^{floxstop\text{-}TeNT}$ allele is described by Zhang *et al.*[30]. Customized primers used to genotype the *Smn*, *Smn*$^{-/-}$, *ChAT*^{Cre}, *Pv*^{Cre} and *Smn*^{Res} alleles are listed in **Supplementary Table 1**. A universal PCR reaction was used as follows: 12.5 µl of GoTaq Hot Start Green Master Mix (Promega), 0.5 µl of each primer (25 µM; Sigma) and 4 µl of 1:20 diluted lysed tail DNA in a final volume of 25 µl using ddH_2O. For the *Smn* and *Smn*^{Res} alleles, products were amplified using the following thermal cycling method: 95 °C for 2 min, followed by 35 cycles of 95 °C for 1 min, 55 °C for 1 min, 72 °C for 1 min and 72 °C for 5 min. For the *Chat*^{Cre} allele: 95 °C for 3 min, 97 °C for 30 s; 2 step cycles 5 times, 95 °C for 15 s, 69 °C for 1 min; 3 step cycles 30 times, 95 °C for 15 s, 60 °C for 15 s, 68 °C for 1 min and 68 °C for 5 min. For the *Pv*^{Cre} allele: 94 °C for 3 min, followed by 35 cycles of 94 °C for 30 s, 58 °C for 30 s, 72 °C for 1 min and 72 °C for 5 min.

Behavioral analysis. Mice from all experimental groups were monitored daily, weighed, and three righting reflex tests were timed and averaged as described previously[13]. Mice with 25% weight loss and an inability to right were euthanized with carbon dioxide to comply with IACUC guidelines. Righting time was defined as the time for the pup to turn over after being placed completely on its back. The cut-off test time for the righting reflex was 60 s to comply with IACUC guidelines. For systemic administration of kainate (Tocris) P0–P4 WT and SMA mice were injected daily subcutaneously with a subconvulsive dose of 1.5 mg/kg dissolved in saline and monitored for body weight and righting times until P4.

Transection experiments. Experiments were conducted on WT mice at P3. Righting times were first evaluated and averaged following three attempts. Subsequently, pups were anesthetized with isoflurane (5% induction and 2.5% maintenance). After a midline incision in the scalp, a transverse slit was opened through the skull with a pair of forceps to visualize the cerebellum. Transections were made with a thin, blunt spatula inserted through the slit. The spatula was inserted caudal to the cerebellum and into the brainstem through the slit. The skin was sutured and the pups were returned to their cage following recovery from anesthesia. The pup's righting ability was evaluated 3 h after transection in the same manner as before transection. At the end of the each experiment, animals were perfused with 4% paraformaldehyde (PFA) transcardially and the brain was removed. Following an overnight fixation, the brain was embedded in 5% agar and sectioned into 100-µm sagittal sections using a vibratome to verify the level and completeness of the transection. Only animals with complete transection at a high medulla level are reported. The sections were imaged unstained with a stereomicroscope equipped with a Zeiss camera.

Physiology using the intact neonatal spinal cord preparation. Experimental protocols used in this study have been described before[13]. Animals were decapitated and the spinal cords dissected and removed under cold (~12 °C) artificial cerebrospinal fluid (aCSF) containing, in mM, 128.35 NaCl, 4 KCl, 0.58 NaH_2PO_4, 21 $NaHCO_3$, 30 D-glucose, 1.5 $CaCl_2$, and 1 $MgSO_4$. The spinal cord was then transferred to a customized recording chamber placed under the objective of an epifluorescence (Leica DM6000FS) or confocal (Leica SP5) microscope. The preparation was perfused continuously with oxygenated (95%O_2, 5%CO_2) aCSF (~10 ml/min). Ventral roots and dorsal roots were placed into suction electrodes for stimulation or recording.

Whole-cell recordings were performed at room temperature (~21 °C) and obtained with patch electrodes advanced through the lateral aspect of the spinal cord (see **Supplementary Fig. 2a**). Patch electrodes were pulled from thin-walled borosilicate glass capillaries with filaments (Sutter Instruments) using a P-1000 puller (Sutter Instruments) to resistances between 5 and 8 MΩ. The electrodes were filled with intracellular solution containing (in mM) 10 NaCl, 130 potassium gluconate, 10 HEPES, 11 EGTA, 1 $MgCl_2$, 0.1 $CaCl_2$, 1 Na_2-ATP, 0.1 Cascade Blue hydrazide (Life Technologies), and in some experiments with 0.5 mg/ml neurobiotin (Vector Labs). pH was adjusted to 7.2–7.3 with KOH; the final osmolarity of the intracellular solution was 295–305 mOsm. Motor neurons were targeted blindly or, in some experiments, from the fluorescence signal following *in vivo* injections of cholera toxin B subunit (CTb) conjugated to a fluorochrome in the IL/QL muscles at birth, after removal of the dura and pia mater from the lateral aspect of the cord over the L2 spinal segments. The identity of recorded neurons as motor neurons was confirmed by evoking an antidromic action potential by stimulation of the cut ventral root (**Supplementary Fig. 2a**). Motor neurons were accepted for further analysis only if the following three criteria were met: (i) stable resting membrane potential of −50 mV or more negative, (ii) an overshooting antidromically evoked action potential and (iii) at least 30 min of recording. The number of animals used for electrophysiology experiments at P2 were 12 WT and 13 SMA animals; at P4, 16 WT, 10 SMA, 8 SMA+Pv^{Cre}, 8 SMA+ChAT^{Cre} and 5 Pv^{TeNT} animals.

For the measurements of passive membrane properties, motor neurons were injected with sequential steps of negative and positive currents for 100 ms in 10-pA steps at −60 mV membrane potential. The input resistance (MΩ) was calculated from the slope of the current/voltage plot within the linear range. Membrane time constants (ms) were calculated as 63% of the maximal negative amplitude during the application of the current pulse[52]. The membrane capacitance (MΩ/ms) of each cell was calculated by dividing the input resistance by the time constant. Measurements were taken from an average of three sweeps. We also determined, for a small number of motor neurons, that the input resistance did not change across the different SMA mouse lines (SMA versus SMA+ChAT^{Cre-} or SMA+Pv^{Cre-}).

Synaptic potentials were recorded from individual motor neurons (DC to 3 kHz, MultiClamp 700B, Molecular Devices) in response to a brief (0.2 ms) orthodromic stimulation (A365, current stimulus isolator, WPI, Sarasota, FL) of a dorsal root (L2 or L5). The stimulus threshold was defined as the current at which the minimal evoked response was recorded in 3 out of 5 trials. The nerve was stimulated at different multiples of threshold. Recordings were fed to an A/D interface (Digidata 1440A, Molecular Devices) and acquired with Clampex (v10.2, Molecular Devices) at a sampling rate of 10 kHz. Data were analyzed off-line using Clampfit (v10.2, Molecular Devices). The monosynaptic component of the EPSP amplitude was measured from the onset of response to 3 ms (ref. 53). Measurements were taken from averaged traces of 5 trials elicited at 0.1 Hz. Bridge balance was applied to all recordings. The liquid junction potential was calculated as −5 mV but was not corrected. Measurements were made on averaged traces (3–5 trials).

Paired-pulse stimulation experiments were performed and analyzed for all experimental groups at P4. The dorsal root was stimulated at 1 Hz for two stimuli and the resulting motor neuron EPSPs were recorded and analyzed off-line. The amplitude of the second EPSP was expressed as a percentage of the first EPSP amplitude. Recording contaminated by spontaneous events or motor neuron depolarizations were discarded.

γ motor neurons were not included in our analysis. γ motor neurons were identified by the presence of an antidromic action potential but lack of direct monosynaptic activation from proprioceptive sensory fibers.

Motor neurons from all experimental groups exhibited a wide range of current required to elicit repetitive firing. To compare statistically the firing frequency in

all experimental groups, we used steps of current (10 pA) above the minimum current required to elicit repetitive firing for 1 s. The firing frequency (Hz) was calculated using the event detection function in Clampfit. The last 3–5 action potentials during repetitive firing (at the end of the spike train), elicited at 90 pA current injection above the current required to elicit repetitive firing, were isolated and averaged using the "event viewer" function in pClamp. Action potential half-width duration (ms) was measured at the half-maximal spike amplitude. The trough voltage of consecutive action potentials was measured at the most negative voltage between two spikes[35]. 1 mM stock solutions of guangxitoxin-1E (GxTX-1E; Alomone) were prepared in ddH_2O and stored at −20 °C. Before electrophysiological recording, 100 nM GxTX-1E was prepared in extracellular solution and administered via the gravity perfusion system for 10 min before recording. We also performed experiments using 200 nM GxTx-1E, but at this concentration we found that GxTx-1E had indirect effects on the input resistance, since subsequent exposure to TTX (1 μM) reversed the increase in the input resistance (data not shown). We did not include in this study any experiments performed with 200 nM GxTx-1E.

The amplitude of the antidromically elicited action potential following ventral root stimulation revealed a significant increase in L2 SMA motor neurons compared to their WT counterparts at P4 (mean ± s.e.m., WT: 75.4 ± 3.0 mV; SMA: 86.4 ± 3.9 mV; $P = 0.02$, Mann–Whitney), consistent with our previous report in L1 SMA motor neurons[13]. In contrast, there was no significant difference in the amplitude of the antidromic action potential between WT and SMA L5 motor neurons (mean ± s.e.m., WT: 76.9 ± 3.8 mV; SMA: 74.1 ± 3.2 mV; $P = 0.85$, unpaired t-test).

After the recording session, in some experiments, the spinal cord was fixed in 4% PFA overnight and subsequently transferred to PBS and processed for immunohistochemistry. In several experiments, intracellularly filled motor neurons from P4 WT and SMA were recovered and detected by means of avidin-biotin complex formation as previously described[53] to measure the somatic area.

At P2, we observed two populations of motor neurons with respect to changes in input resistance and time constant. We divided these two groups by applying the following criteria and termed them as "affected" and "unaffected" SMA motor neurons. Unaffected SMA motor neurons were defined as those SMA motor neurons that exhibited similar correlation between input resistance and time constant to those observed in WT motor neurons. Conversely, affected SMA motor neurons were those motor neurons exhibiting higher values of input resistance and time constant (**Supplementary Fig. 2b**).

Relationship between EPSP amplitude and input resistance. This relationship was investigated in our previous study[13]. Computer modeling studies have been used to examine the effect of input resistance on the amplitude of monosynaptic EPSPs recorded in adult cat motor neurons in response to stimulation of muscle spindle afferents[54]. The EPSP amplitude is almost linearly proportional to the motor neuron input resistance, so that a 3-fold increase in input resistance leads to a 2.8-fold increase in the EPSP amplitude. The input resistance of SMA motor neurons examined in this study is ~3 times that of WT motor neurons, which will amplify the synaptic potential for a given synaptic current by ~3.7 fold according to the model described by Lev-Tov *et al.*[54]. Therefore, the ~5 fold reduction in the amplitude of primary afferent-evoked synaptic potentials in SMA motor neurons actually reflects a much greater reduction (~18 fold; i.e., 5 × 3.7) in the amplitude of the synaptic currents, which is in agreement with our previous study[13].

Functional assessment of the NMJ. To functionally assess neuromuscular junctions of the QL muscle at P4, we developed a technique by which motor neurons axons in the ventral root L2 supplying the QL muscle were stimulated by drawing the ventral root into a suction electrode, having removed the spinal cord, and recorded the compound muscle action potential (CMAP) from the muscle using a concentric bipolar electrode. L2 motor neuron axons were stimulated with a single stimulus at 0.1 Hz or at 20 Hz to emulate the physiological range of neonatal motor neuron firing. The maximum CMAP amplitude (baseline-to-peak) was measured from 3–5 averages.

Somatodendritic labeling of motor neurons. Experimental protocols used in this study have been described before[13]. 101 mice 0–11 d old were used in tracing and immunohistochemistry experiments (24 WT, 21 SMA, 21 SMA+Pv^{Cre}, 17 SMA+$ChAT^{Cre}$, 12 SMA+$(Pv+ChAT)^{Cre}$, 6 Pv^{TeNT}). The spinal cord was transferred to a dissection chamber and the L2 or L5 ventral root was placed inside a suction electrode and backfilled with a fluorescent dextran to label the motor neurons (**Supplementary Table 2**). Spinal cords from P0–P5 animals were intact while P11 spinal cords were hemisected to improve oxygenation. The cord was perfused with cold (~10 °C), oxygenated (95% O_2, 5% CO_2) aCSF (containing, in mM, 128.35 NaCl, 4 KCl, 0.58 NaH_2PO_4, 21 $NaHCO_3$, 30 D-glucose, 0.1 $CaCl_2$ and 2 $MgSO_4$). After 12–16 h the cord was immersion-fixed in 4% PFA and washed in 0.01 M phosphate-buffered saline (PBS). Sections were subsequently processed for immunohistochemistry as described below and in **Supplementary Table 2**.

Retrograde labeling of muscle-identified motor neurons. Motor neurons supplying the IL and QL muscles were retrogradely labeled *in vivo* by intramuscular injection of CTb conjugated to Alexa 488. Newborn (P0) mice were anesthetized by isoflurane inhalation. A small incision in the left iliac (inguinal) area was made to access the IL/QL muscles, taking care not to puncture the peritoneum. The muscles were injected with ~1 μl of 1% CTb-Alexa 488 in PBS using a finely pulled glass micropipette. The CTb was delivered by pressure to an adapted microsyringe. The incision was closed with sutures. The spinal cord was taken at P4 following verification by fluorescence of accurate injection of CTb in the muscles and processed for immunohistochemistry.

Overexpression of BDNF in SMA mice. SMA mutant mice at P0 were anesthetized by isoflurane (by inhalation) and injected intracerebroventricularly with 10 μl of 7.5×10^{13} GC/ml AAV2/9-CMV-GFP-2A-mBDNF virus (Vector BioLabs) at birth (P0), using a modified Hamilton syringe. Pups were allowed to recover from anesthesia for 30 min before being returned to the cage. Mice were sacrificed at P5 for physiological or morphological experiments. For morphological experiments, the spinal cord and lumbar dorsal root ganglia (DRGs) were immersion-fixed in 4% PFA overnight. The L2 spinal segments and L2 DRGs were cut in 70-μm-thick sections using a vibratome. GAD65 and GAD67 antibodies (kind gift from the T. Jessell laboratory) were used, together with the VGluT1 antibody, to visualize GABApre synapses on $VGluT1^+$ synapses in SMA mice injected with AAV9-BDNF and SMA controls, as in ref. 32. GFP was amplified using chicken anti-GFP (Aves Labs; **Supplementary Table 3**) at a 1:1,000 concentration following overnight incubation. The anti-GFP was visualized with donkey anti-chicken Alexa-488 secondary antibody (**Supplementary Table 3**) for 3 h. The sections were scanned at the confocal microscope. Details and the effectiveness of the method are included in our previous study[32].

Immunohistochemistry. Some immunohistochemical protocols used in this study have been previously described[13,32]. Details for new fixatives and immunohistochemical protocols used in this study are included in **Supplementary Tables 2** and **3**. All antibodies except the VGluT1 one are commercially available. Antibody to mouse VGluT1 was produced in guinea pig by Covance against the epitope (C)GATHSTVQPPRPPPP, which lies within the N terminus of mouse VGluT1. The antibody was validated in $VGluT1^{-/-}$ mouse tissue. Spinal cords were embedded in warm 5% agar and serial transverse sections were cut on a vibratome (75 μm thickness). Sections were blocked with 10% normal donkey serum in 0.01 M PBS with 0.1% Triton X-100 (PBS-T; pH 7.4) and incubated overnight at room temperature in different combinations of antisera in PBS-T (**Supplementary Table 2**). For experiments involving anti-mouse antibodies, sections were preincubated for 1 h in M.O.M blocker (Vector Laboratories) in PBS-T to block endogenous antigens. The following day, sections were washed in PBS-T and secondary antibody incubations were performed for 3 h with the appropriate species-specific antiserum diluted in PBS-T. Sections were subsequently washed in PBS and mounted on glass slides using Vectashield (Vector Laboratories).

For the Kv2.1 immunoreactivity experiments, we used the K89/34 mouse IgG1 antibody (NeuroMab; mAb binds within aa 837–853; cat #73-014 RRID: AB10672253). For the Kv2.2 immunoreactivity experiments, we used the N372B/1 mouse IgG1 antibody (NeuroMab; mAb binds within aa 764 –907, cat#73-369, RRID:AB_2315869). Both antibodies have been verified to be specific by testing on Kv2.1 and Kv2.2 knockout mice[55] (see also, for Kv2.1, http://neuromab.ucdavis.edu/datasheet/K89_34.pdf; for Kv2.2, http://neuromab.ucdavis.edu/datasheet/N372B_1.pdf). We also verified specificity of the Kv2.1 immunoreactivity on Kv2.1 knockout mouse spinal cord (kind gift from J. Trimmer).

doi:10.1038/nn.4561

Neuromuscular junctions (NMJs) were analyzed in the QL muscle (**Supplementary Table 2**). Muscles from P4 mice from each genotype were fixed with 4% PFA for 20 min and transferred to PBS. Single fibers were teased out using fine forceps and washed for 30 min in PBS supplemented with 0.1 M glycine. Fibers were incubated with α-bungarotoxin-555 antibody (**Supplementary Table 3**) for 20 min and washed in PBS before permeabilization with ice-cold methanol at −20 °C for 2 min. Fibers were washed in PBS and incubated in a blocking solution containing 10% donkey serum in 0.3% PBS-T for 1 h before treatment with anti-neurofilament and anti-synaptophysin (**Supplementary Table 3**) at 4 °C overnight. Samples were washed with PBS before incubation with the appropriate secondary antibodies for 1 h (**Supplementary Table 2**). Fibers were washed and mounted in Vectashield.

The sources and catalog numbers for all primary and secondary antibodies are shown in **Supplementary Table 3**.

Imaging and analysis. Sections were imaged using an SP5 Leica confocal microscope and analyzed using LASAF software (Leica). For all immunohistochemical analysis, at least three animals were used for each genotype. For SMN quantification, the number of motor and proprioceptive neurons with either present or absent nuclear Gems from L1–L3 spinal segments were counted using a ×40 objective from *z*-stack (0.5-µm step) scans. At least 30 motor and proprioceptive neurons were included from each animal for each genotype. For motor neuron counts, we analyzed *z*-stacks images (at 3-µm intervals) collected for each section that contained a fluorescent signal from L2 retrogradely labeled motor neurons as previously described for L1 motor neurons[13]. Sections were scanned using a ×20 objective. Only motor neurons ($ChAT^+$) that contained the nucleus were counted in order to avoid double counting of adjoining sections.

Quantitative analysis of VGluT1-immunoreactive synaptic densities on motor neurons at P4 and P11 were performed on stacks of optical sections scanned using a ×40 objective throughout the whole section thickness at 0.35-µm *z*-steps to include the whole cell body and dendrites of retrogradely labeled and $ChAT^+$ motor neurons. To obtain density estimates, we measured all $VGluT1^+$ contacts on dendritic segments at 50-µm sequential distances (0–50, 50–100 and 100–150 µm) from the cell body and divided this number by the total linear length of all dendritic segments in each compartment as described previously[13]. For VGluT1 motor neuron soma counts, only motor neurons with a whole cell body present in the *z*-stack were included.

To determine the extent of NMJ innervation, NMJ synapses were acquired using a ×20 objective and *z*-stack images were scanned at 2-µm intervals. Images were analyzed off-line using LASAF software. NMJs were only considered innervated if the presynaptic nerve terminal completely colocalized with the postsynaptic endplate.

Analysis of Kv2.1 and Kv2.2 channels were performed from single-optical-plane images acquired with a ×63 oil objective at 4,096 × 4,096 dpi resolution using an SP5 Leica confocal microscope. Only motor neuron somata (identified by ChAT immunoreactivity) in which the nucleus was present were included in the analysis. To calculate the coverage by Kv channel on motor neuron soma, a line was drawn along the soma perimeter to acquire the fluorescence intensity (expressed in arbitrary units), avoiding the area in which primary dendrites were present using LAS X software (Leica). A baseline fluorescence intensity measurement was achieved by drawing a straight line in the cytoplasm. The fluorescence intensity measurements were exported into Excel as *x*-*y* coordinates (*x*: distance in µm; *y*: fluorescence intensity in arbitrary units). Fluorescence signal more than 3 s.d. above the baseline intensity measurement was considered expression of Kv immunoreactivity along the soma perimeter (**Supplementary Fig. 14c**), whereas the signal below was considered as background. The distance with fluorescence intensity above 3 s.d. was calculated for each motor neuron and Kv channel coverage was expressed as a percentage of the total perimeter of the motor neuron soma.

Staining intensity measurements. Images of synaptic terminals were acquired on a Leica SP8 confocal microscope using a 40× objective with 5× digital zoom at a 2,048 × 2,048 optical resolution. Acquisition settings for excitation and fluorescence detection parameters were identical for each genotype, SMA controls and SMA+AAV9-BDNF. The GAD65 and GAD67 terminals were analyzed within a 10-µm confocal *z*-stack at 300-nm step intervals. Surface area and staining intensities were determined using Leica LAS AF imaging software. Relative synaptic protein levels were quantified by assessing the mean gray values, defined as the sum of the gray values of all the pixels in a region of interest (pixel sum) divided by the number of pixels in that region (pixel count), as we reported recently[32]. Regions of interest were defined as the outline of positively stained terminals. To quantify the relative levels of GABApre synaptic proteins (GAD65 and GAD67), only varicosities directly juxtaposed to proprioceptive afferent terminals ($VGluT1^+$) were considered.

Western blot analysis. The ventral horns from L1–L3 spinal cords of WT and SMA mice ($n = 2$) at P4 were removed under the microscope. Tissue was homogenized in lysis buffer (150 mM NaCl, 1% Triton, 2 mM EDTA, 50 mM Tris, pH 7.4). Protein extract (20 µg) was electrophoresed on a 12% SDS–PAGE gel and blotted for 40 min to a PVDF membrane. The membranes were blocked for 1 h with 5% skim milk and then probed with mouse anti-SMN (1:10,000, B&D), mouse anti-tubulin (1:50,000, clone DM1A, Sigma) and mouse anti-Kv2.1 (1:5, NeuroMab; **Supplementary Table 3**) in blocking buffer overnight at 4 °C. Subsequently, the membranes were washed 3 times with PBS and incubated with appropriate HRP-conjugated secondary antibodies (Jackson ImmunoResearch Laboratories; **Supplementary Table 3**) in PBS-T for 1 h at room temperature. After three sequential 10-min washes, enhanced chemiluminescence (GE Healthcare, Lifesciences) was used to for visualization.

Statistics. Results are expressed as means ± s.e.m. Statistical analysis was performed using GraphPad Prism 6. Comparison was performed by either Student's *t*-test or one-way ANOVA (*post hoc* comparison methods are indicated in the Results and figure legends when necessary). Results were considered statistically significant if $P < 0.05$. The D'Agostino and Pearson omnibus normality test was used to assess the normality for all data. If violated, non-parametric tests were used. No statistical methods were used to predetermine sample sizes, but our sample sizes are similar to those reported in previous publications[13,20,41,53]. No randomization was used. Data collection and analysis were not performed blind to the conditions of the experiments. A **Supplementary Methods Checklist** is available.

Data availability. The data that support the findings of this study are available from the corresponding author upon reasonable request.

51. Hippenmeyer, S. *et al.* A developmental switch in the response of DRG neurons to ETS transcription factor signaling. *PLoS Biol.* **3**, e159 (2005).
52. Isokawa, M. Membrane time constant as a tool to assess cell degeneration. *Brain Res. Brain Res. Protoc.* **1**, 114–116 (1997).
53. Shneider, N.A., Mentis, G.Z., Schustak, J. & O'Donovan, M.J. Functionally reduced sensorimotor connections form with normal specificity despite abnormal muscle spindle development: the role of spindle-derived neurotrophin 3. *J. Neurosci.* **29**, 4719–4735 (2009).
54. Lev-Tov, A., Miller, J.P., Burke, R.E. & Rall, W. Factors that control amplitude of EPSPs in dendritic neurons. *J. Neurophysiol.* **50**, 399–412 (1983).
55. Bishop, H.I. *et al.* Distinct cell- and layer-specific expression patterns and independent regulation of Kv2 channel subtypes in cortical pyramidal neurons. *J. Neurosci.* **35**, 14922–14942 (2015).

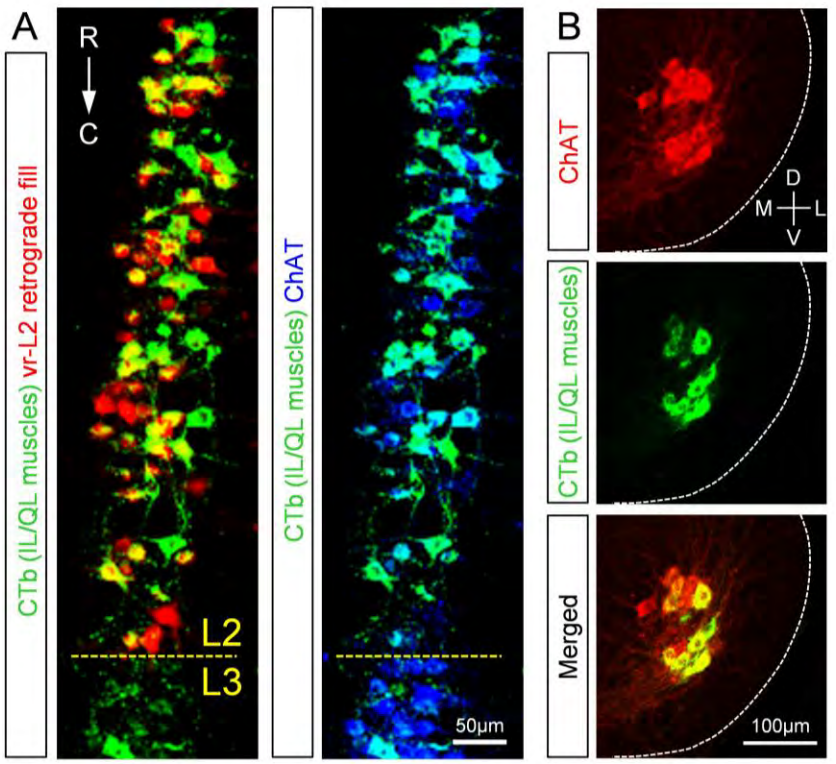

Supplementary Figure 1

Iliopsoas and quadratus lumborum motor neurons in the L2 spinal segment.

(A) IL and QL motor neurons were labeled after CTb-488 (green) muscle injections at birth. At P4, the L2 motor neurons were retrogradely filled with Texas Red Dextran (red) using the ex vivo spinal cord preparation to identify the rostral and caudal borders (dotted line) of the L2 spinal segment. IL and QL motor neurons (CTb-488, green) were quantified as a percentage of ChAT (blue) immunoreactive motor neurons. (B) Transverse sections of the L2 motor neuron nucleus containing IL/QL motor neurons (CTb-488, green) and ChAT immunoreactivity (red). Merged image is shown at the bottom. R: rostral, C: caudal, D: dorsal, V: ventral, M: medial, L: lateral.

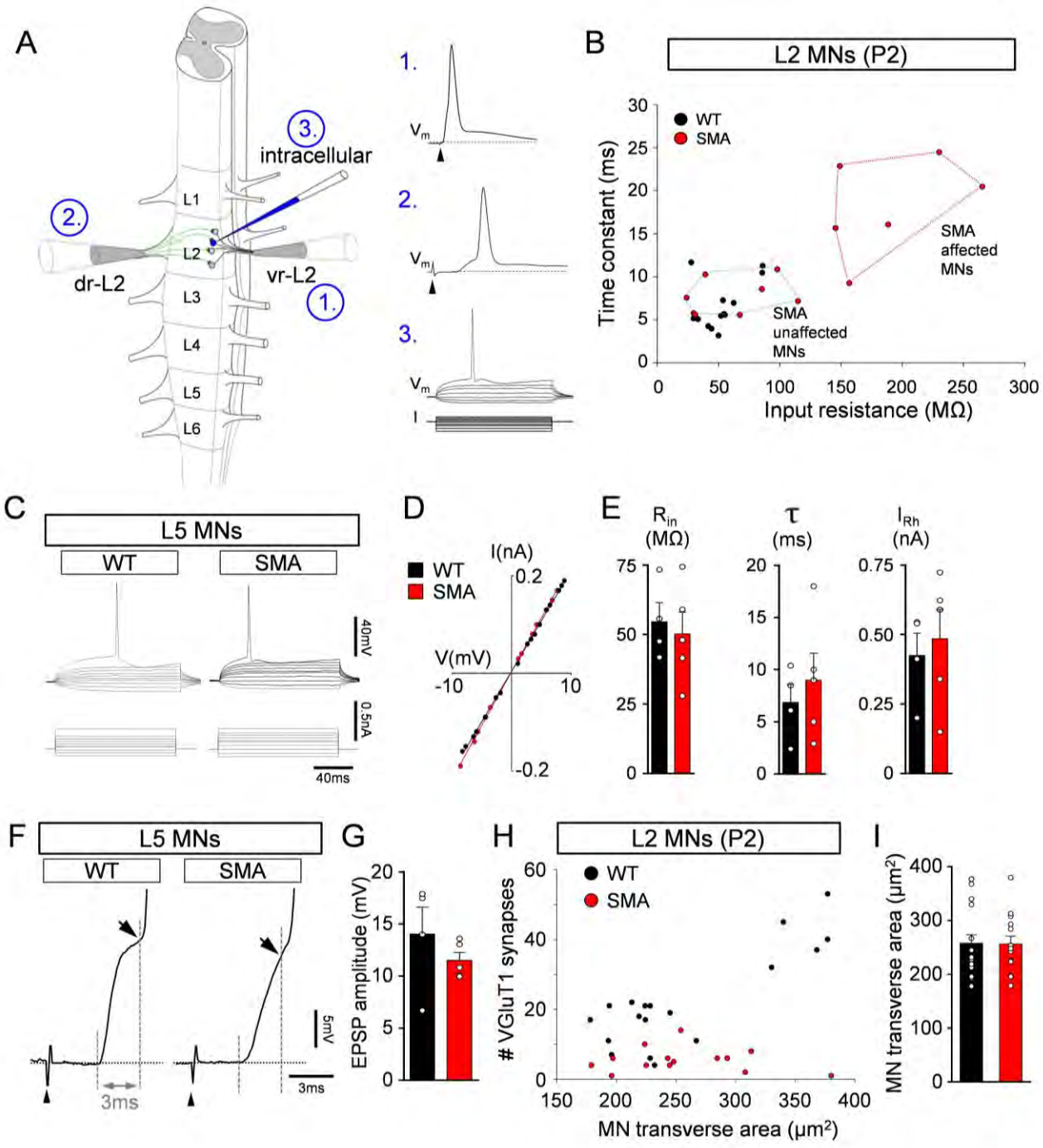

Supplementary Figure 2

Resistant (L5) SMA motor neurons are not hyperexcitable, whereas vulnerable (L2) SMA motor neurons exhibit the first signs of dysfunction at P2.

(A) Schematic of experimental protocol. Extracellular electrodes in the L2 ventral root (1) and L2 dorsal root (2) were used for stimulation. Responses from individual motor neurons were recorded intracellularly (3) (whole-cell patch clamp) using the intact ex vivo spinal cord preparation. Traces on the right show: an antidromically evoked action potential following ventral root stimulation (1), a synaptic response from a motor neuron following dorsal root stimulation (2) and current-to-voltage relationship in whole-cell

configuration (3).

(B) Input resistance-time constant relationship for L2 WT and SMA motor neurons at P2. The SMA-affected motor neurons exhibit high input resistance and high values of time constant (marked by red dotted lines). The SMA-unaffected motor neurons exhibit similar values of input resistance and time constant with WT motor neurons (marked by blue dotted lines).

(C) Membrane responses following current injections in a WT and an SMA L5 motor neuron at P4.

(D) Current/voltage relationships for the two motor neurons shown in (C).

(E) The average input resistance (R_{in}), membrane time constant (τ) and rheobase current (I_{Rh}) for WT (n=4) and SMA (n=5) L5 motor neurons at P4.

(F) Intracellular responses to supramaximal stimulation of the L5 dorsal root in a WT and a SMA motor neuron at P4. The peak amplitude of monosynaptic EPSP is indicated by arrows. The arrowheads show the stimulus artifact.

(G) The average peak EPSP amplitude for WT (n=4) and SMA (n=5) L5 motor neurons.

(H) Relationship between transverse area of L2 motor neurons and the number of VGluT1 synapses in WT and SMA motor neurons at P2.

(I) The average transverse area of WT and SMA motor neurons at P2.

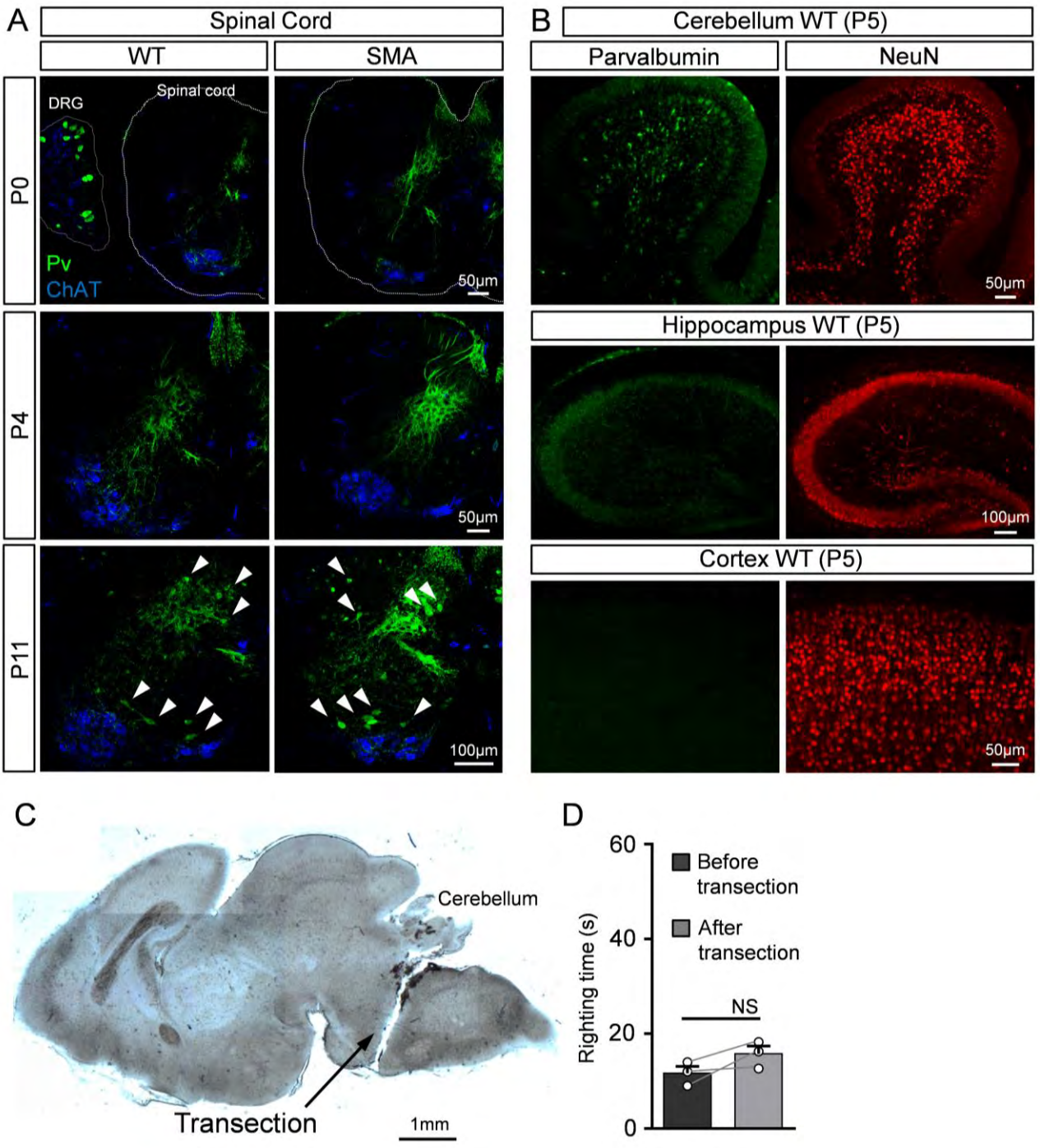

Supplementary Figure 3

Parvalbumin expression in the spinal cord and brain during first postnatal week.

(A) Transverse sections from WT and SMA spinal cords at P0, P4 and P11 showing parvalbumin (green) and ChAT (blue) immunoreactivity. Arrows indicate parvalbumin+ interneurons at P11. DRG: dorsal root ganglion.

(B) Parvalbumin (green) and NeuN (red) expression in the cerebellum, hippocampus and cortex in P5 WT mice.

(C) Sagittal section of the brain following transection at a high medulla level in a P3 WT mouse. Arrow indicates the level of complete

transection.

(D) Average righting times before and 3 hours after transection. NS: no significant difference (p=0.20, Mann-Whitney test).

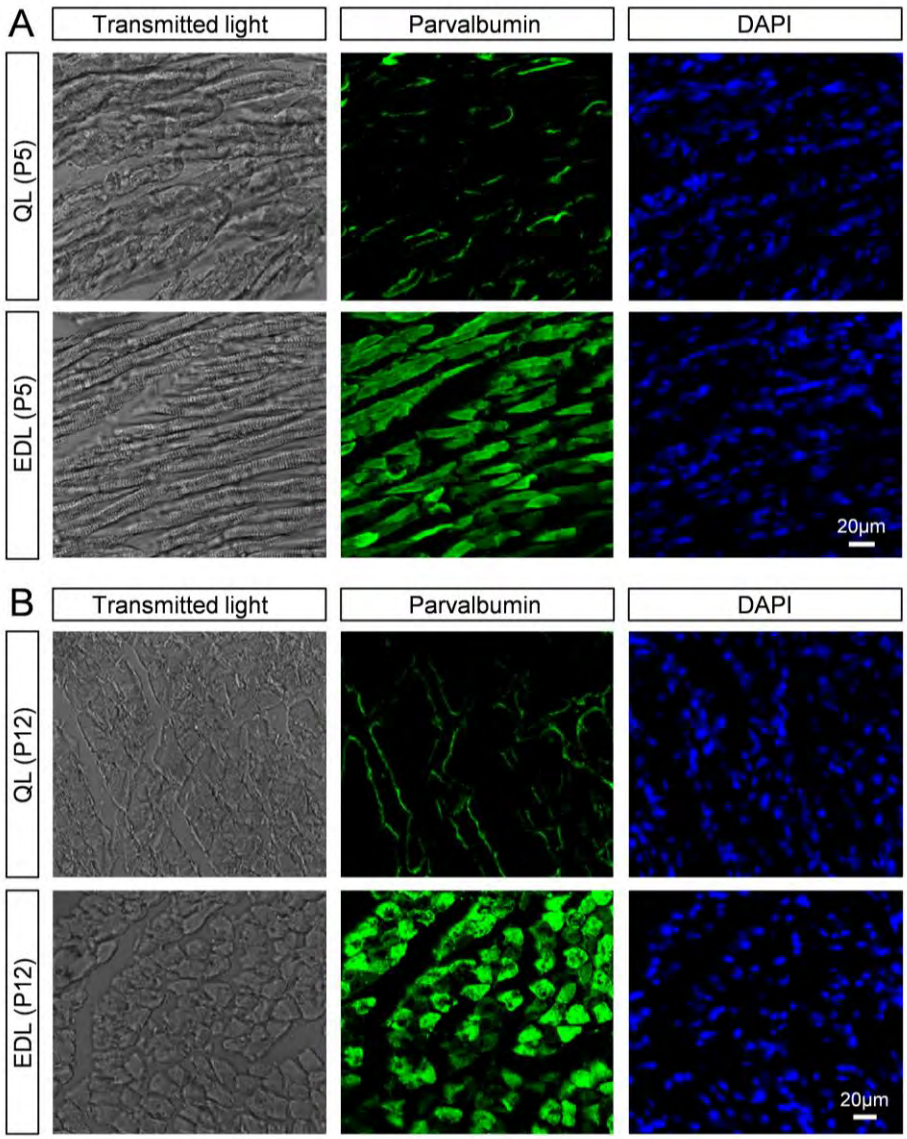

Supplementary Figure 4

Absence of parvalbumin from the quadratus lumborum muscle during the first 2 postnatal weeks.

Sections from QL and EDL muscles immunoreacted against parvalbumin at P5 (A) and P12 (B). Nuclear stain DAPI in blue.

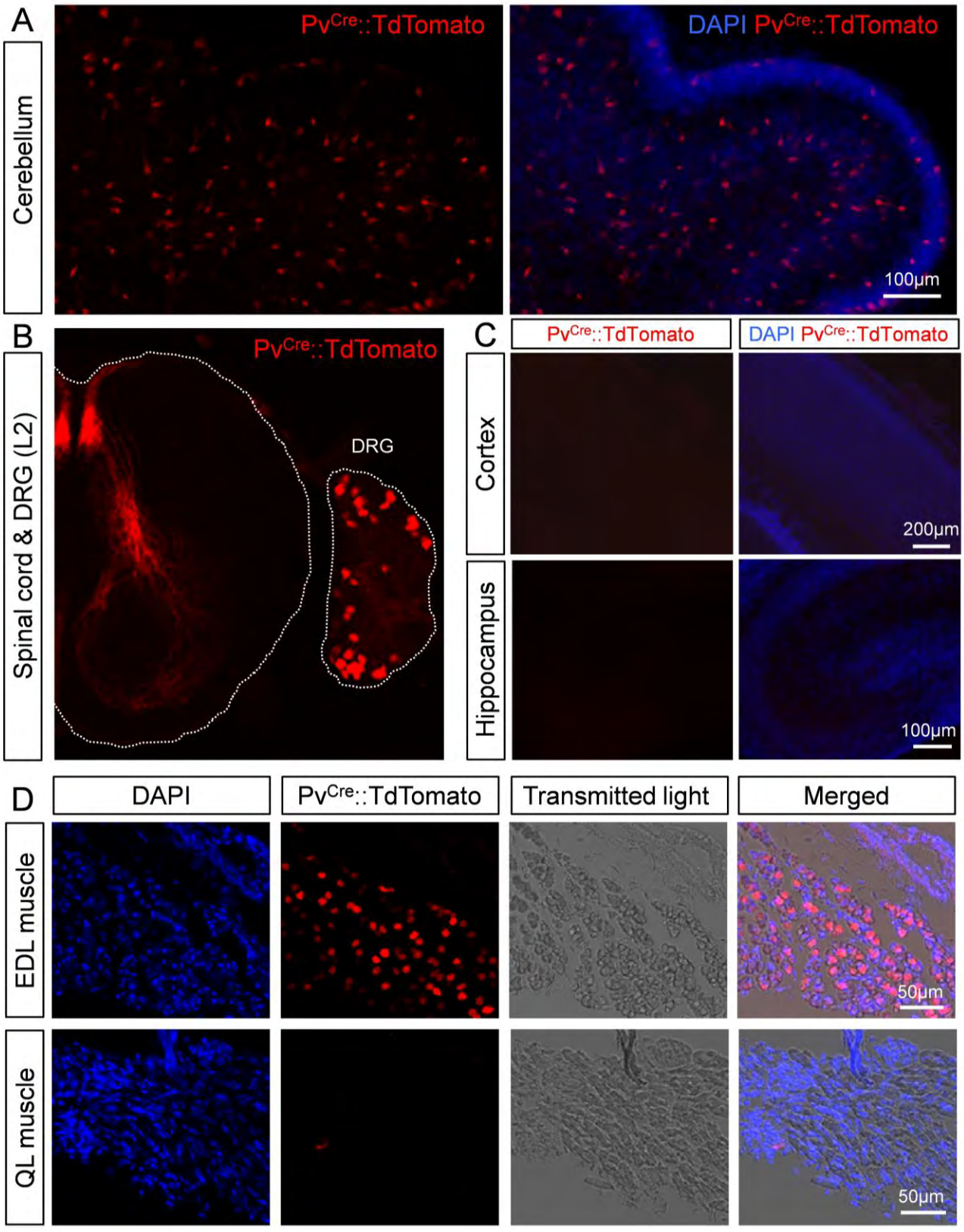

Supplementary Figure 5

Expression of the fluorescent reporter TdTomato in Pv^{Cre} mice.

Expression of TdTomato (red) and DAPI (blue) in cerebellum (A), spinal cord and DRG in the L2 segment (B) and its absence in cortex and hippocampus (C).(D) shows examples from EDL and QL muscles. TdTomato was only observed in EDL muscle.

Nature Neuroscience: doi:10.1038/nn.4561

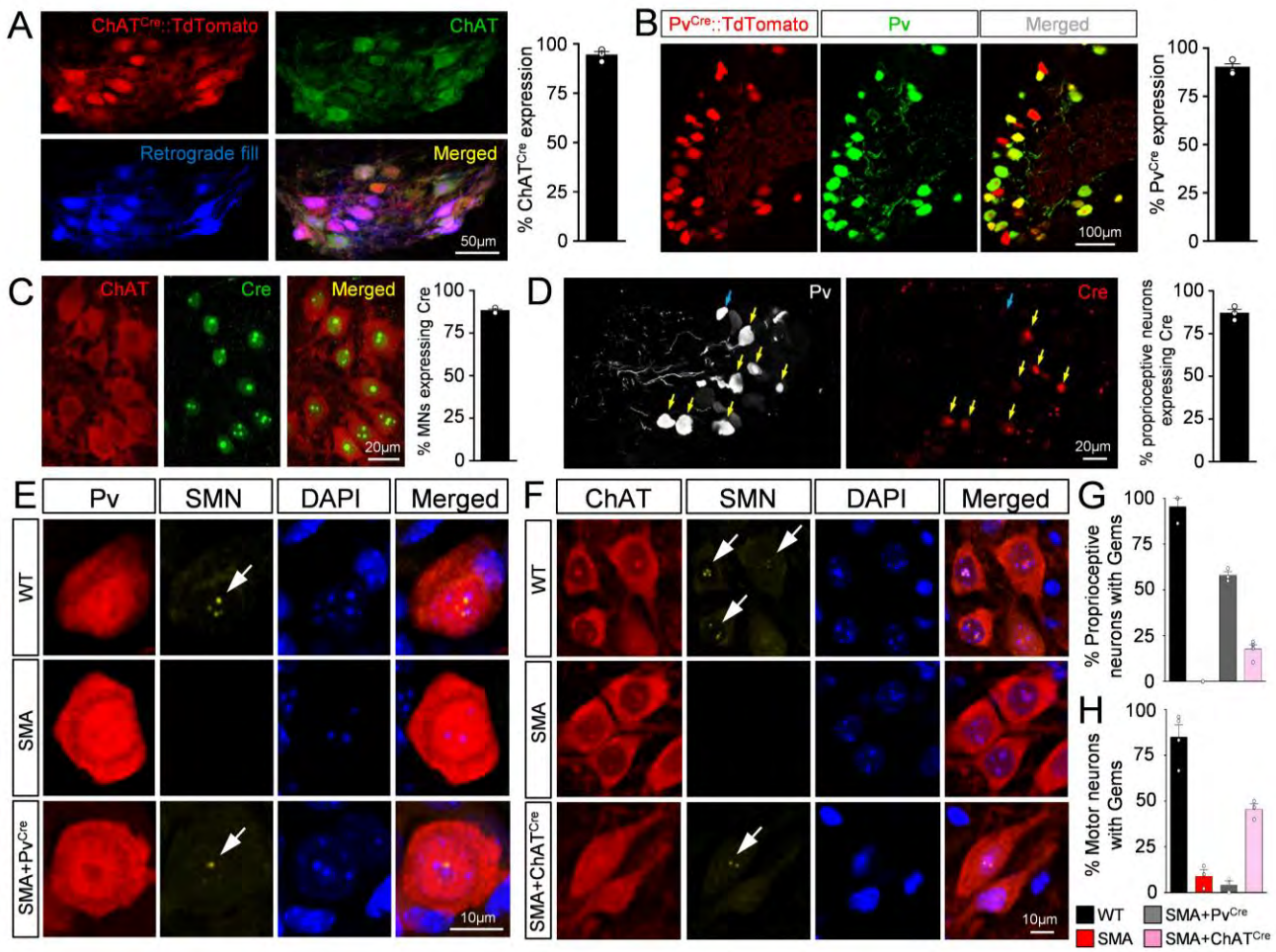

Supplementary Figure 6

Validation of selective upregulation of SMN protein in proprioceptive and motor neurons

(A) Confocal images from L2 spinal segment at P11 showing motor neurons expressing TdTomato (red) driven by ChAT::Cre, ChAT immunoreactivity (green) and retrogradely filled motor neurons with Cascade Blue Dextran (blue) from the ventral root and their merged image. Graph shows the percentage expression of TdTomato+ to ChAT+ motor neurons.

(B) Confocal images from an L2 dorsal root ganglion at P11 showing TdTomato (red) expression driven by Pv^{Cre}, Parvalbumin (Pv) immunoreactivity (green) and their merged image. Graph shows the percentage expression of TdTomato+ to Paralbumin+ neurons.

(C) Confocal images from L2 ChAT+ motor neurons (red) and Cre immunoreactivity (green) in $ChAT^{Cre}$ mice at P11 and their merged image. Graph indicates the percentage of ChAT+ motor neurons expressing Cre.

(D) Confocal images from an L2 dorsal root ganglion showing Parvalbumin (white) and Cre (red) immunoreactivity in Pv^{Cre} mice at P11. Yellow arrows indicate co-localization and blue arrow indicates no co-localization. Graph indicates the percentage of Parvalbumin+ neurons expressing Cre.

(E) Expression of Gems (arrows) revealed by SMN immunoreactivity (yellow) in nuclei (nuclear stain DAPI in blue) of proprioceptive neurons labeled by parvalbumin (red) in L2 dorsal root ganglia in WT, SMA and SMA+Pv^{Cre} mice at P4.

(F) Similar to (A) but for motor neurons labeled by ChAT immunoreactivity (red) in the L2 segment of the spinal cord in WT, SMA and SMA+$ChAT^{Cre}$ mice at P4.

(G) The average percentage expression of Gems in proprioceptive neurons in WT, SMA, SMA+Pv^{Cre} and SMA+$ChAT^{Cre}$ mice at P4.

(H) The average percentage expression of Gems in motor neurons in WT, SMA, SMA+Pv^{Cre} and SMA+$ChAT^{Cre}$ mice at P4.

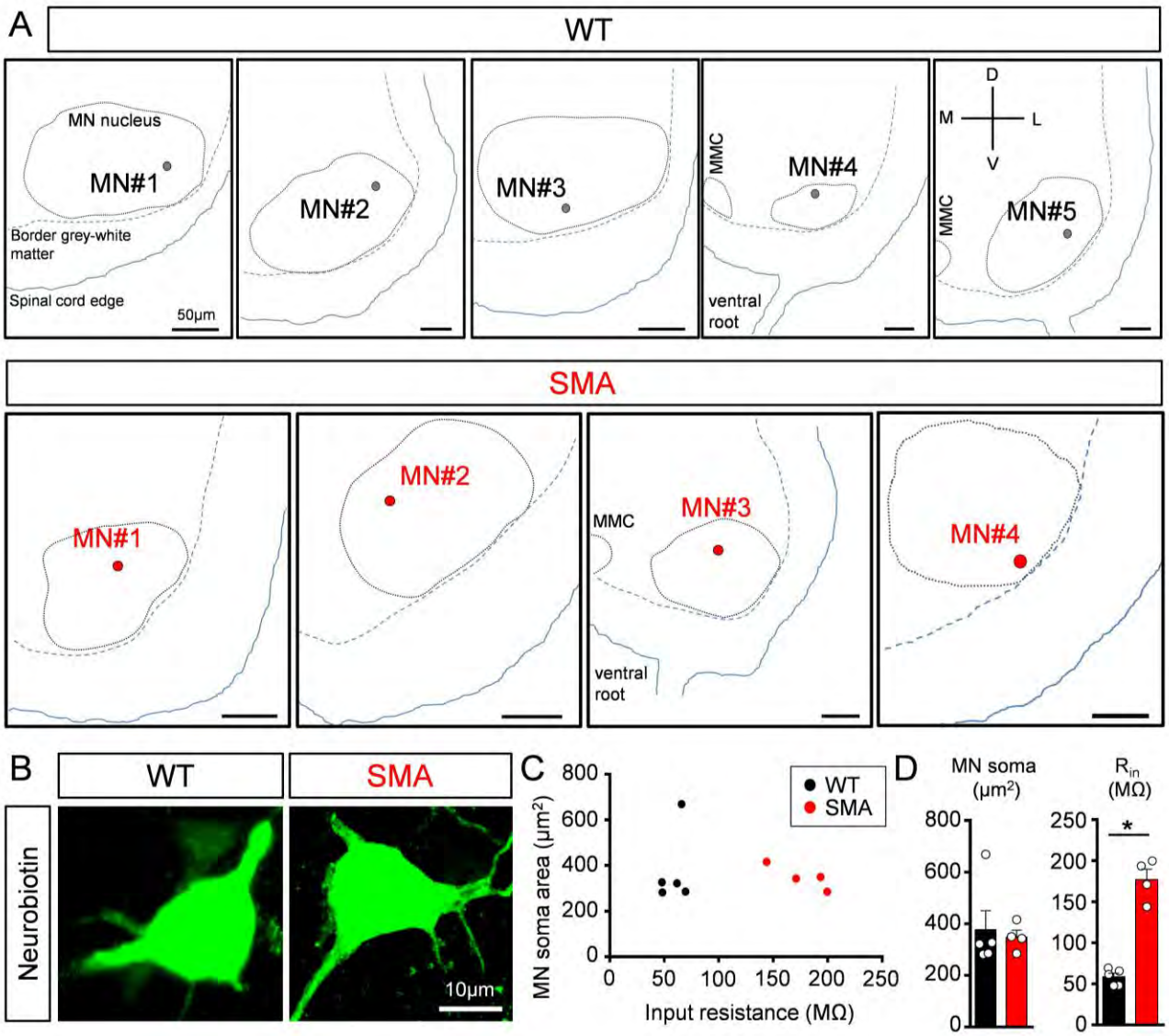

Supplementary Figure 7

Changes in motor neuron input resistance do not depend on motor neuron soma size.

(A) Location of intracellularly recorded L2 WT and SMA motor neurons within the motor neuron nucleus at P4. The grey line indicates the approximate border of the motor neuron nucleus. The blue dotted line indicates the approximate grey-white matter border. The solid blue line indicates the edge of the spinal cord. The location of the medial motor nucleus (MMC) is noted in a few instances. Scale bars: 50 µm. D: dorsal, V: ventral, M: medial, L: lateral.

(B) Confocal images (single optical plane) of a WT and an SMA P4 L2 motor neuron filled with Neurobiotin following intracellular recording. Scale bar applies to both images.

(C) Graph shows the relationship between the input resistance and the corresponding soma size for 5 WT and 4 SMA motor neurons.

(D) Average soma size (left graph) and input resistance (right graph) for the WT and SMA motor neurons shown in (C). * P= 0.02, t-test.

All data are represented as mean ± s.e.m. For details, see online methods checklist.

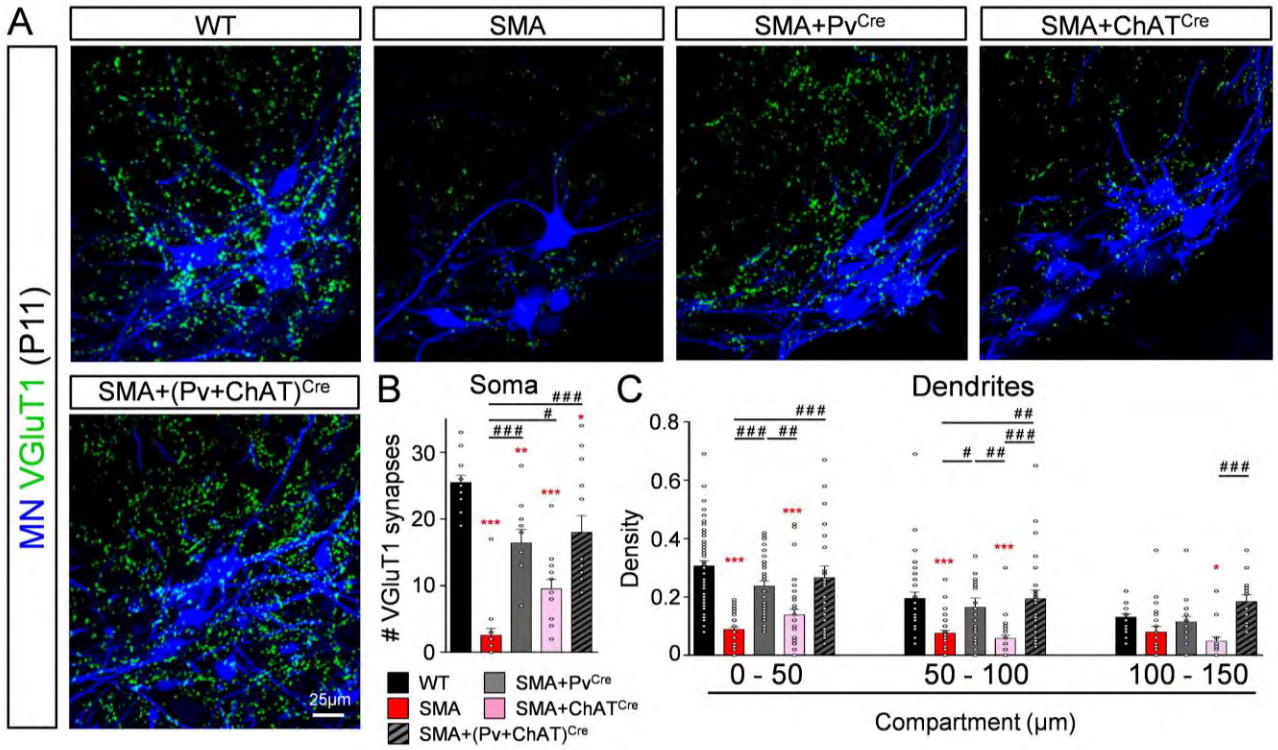

Supplementary Figure 8

Maintenance of rescued VGluT1 synapses at P11.

(A) Z-stack projection of confocal images from retrogradely labeled L2 motor neurons (blue) and VGluT1 synaptic boutons (green) from WT, SMA, SMA+Pv^{Cre}, SMA+ChAT^{Cre} and SMA+(Pv+ChAT)^{Cre} mice at P11. The total distance in the z-axis for all images was 7 μm (20 optical planes at 0.35 μm intervals).

(B) The average number of VGluT1 boutons on somata of L2 WT, SMA, SMA+Pv^{Cre}, SMA+ChAT^{Cre} and SMA+(Pv+ChAT)^{Cre} motor neurons at P11. # P<0.05, ## P<0.01, ### P<0.001, one-way ANOVA, Tukey's *post hoc* analysis [SMA v SMA+Pv^{Cre}, SMA v SMA+ChAT^{Cre} and SMA v SMA+(Pv+ChAT)^{Cre}]. * P<0.05, ** P<0.01, *** P<0.001, one-way ANOVA, Tukey's *post hoc* analysis [WT v SMA, WT v SMA+Pv^{Cre}, SMA v SMA+ChAT^{Cre} and WT v SMA+(Pv+ChAT)^{Cre}]. All data are represented as mean ± s.e.m. For details, see online methods checklist.

(C) VGluT1 synaptic density on 50 μm dendritic compartments from the soma, for the same groups shown in (B). # P<0.05, ## P<0.01, ### P<0.001, one-way ANOVA, Tukey's *post hoc* analysis [SMA v SMA+Pv^{Cre}, SMA v SMA+ChAT^{Cre} and SMA v SMA+(Pv+ChAT)^{Cre}]. *** P<0.001, one-way ANOVA, Tukey's *post hoc* analysis [WT v SMA, SMA v SMA+ChAT^{Cre}]. All data are represented as mean ± s.e.m. For details, see online methods checklist.

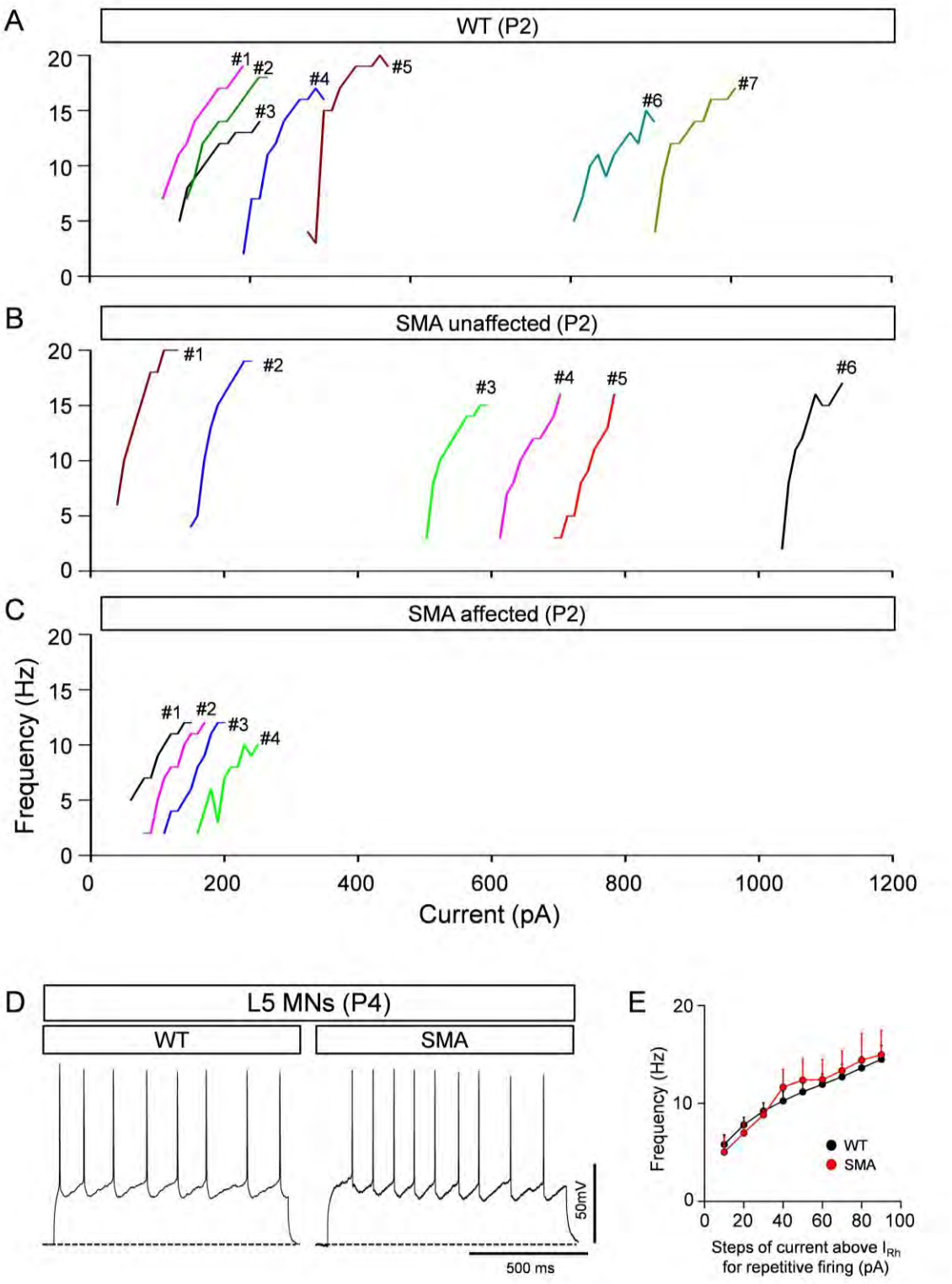

Supplementary Figure 9

Variability in rheobase, required for motor neuron repetitive firing at P2, and absence of changes in firing frequencies for resistant SMA motor neurons at P4.

(A) Frequency to current plots for seven WT motor neurons at P2.

(B) Frequency to current plots for six SMA-unaffected motor neurons at P2.

(C) Frequency to current plots for four SMA-affected motor neurons at P2.

(D) Repetitive firing following 50 pA current injection above the minimum current required for continuous spiking, in a WT and an SMA L5 motor neuron at P4.

(E) Frequency-to-current relationships for the two groups shown in (D).

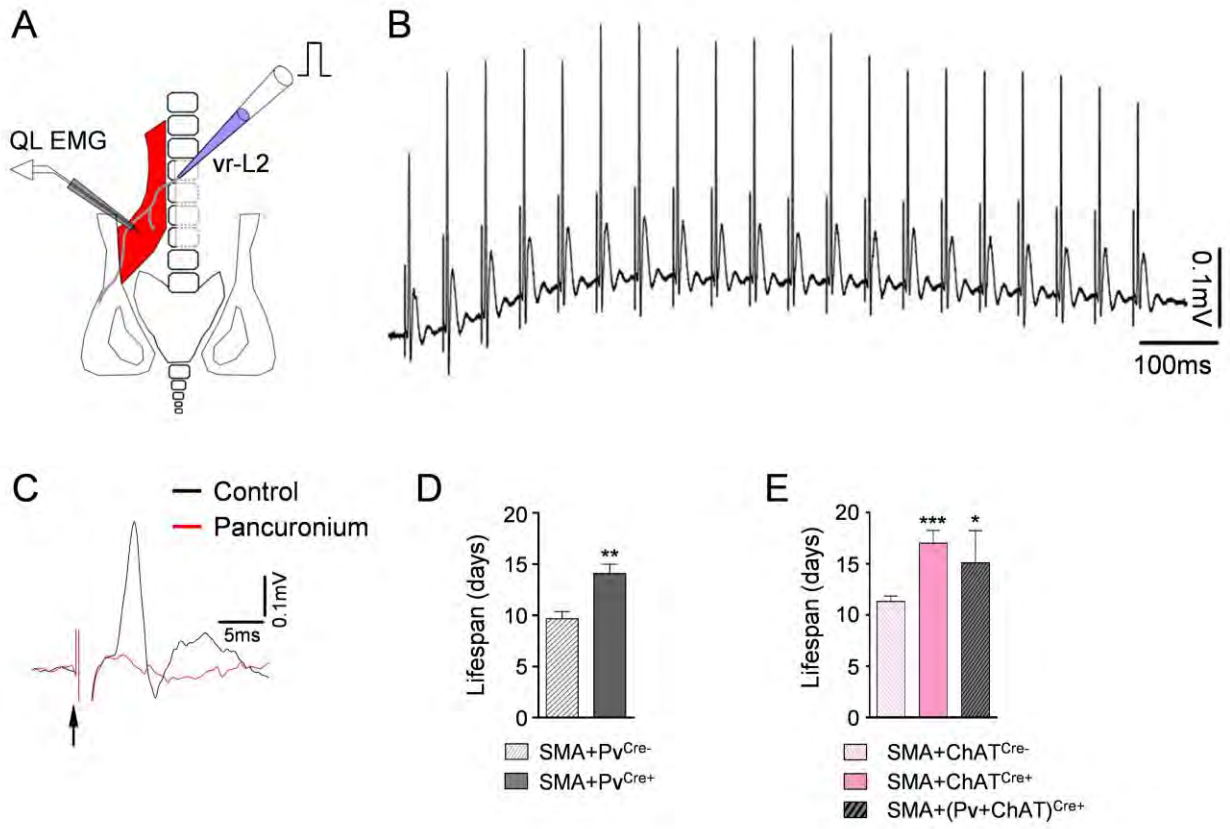

Supplementary Figure 10

NMJ functional assays and lifespan of SMA mice with selective restoration of SMN in either proprioceptive neurons, motor neurons or both neuronal classes.

(A) Schematic showing the set-up used to record the compound muscle action potential (CMAP) from the QL muscle following stimulation of the L2 ventral root at P4.

(B) CMAP responses at 20 Hz stimulation frequency.

(C) CMAP response before (black) and after 30 μM pancuronium (red). Arrow indicates the stimulus artifact.

(D) Average lifespan in SMA+Pv^{Cre+} compared to SMA+Pv^{Cre-} mice. ** P=0.013, unpaired t-test.

(E) Average lifespan in SMA+$ChAT^{Cre+}$ and SMA+$(Pv+ChAT)^{Cre+}$ compared to SMA+$ChAT^{Cre-}$ mice. * P<0.05, one-way ANOVA, Tukey's *post hoc* analysis SMA+$ChAT^{Cre-}$ v SMA+$ChAT^{Cre+}$; *** P<0.001, one-way ANOVA, Tukey's *post hoc* analysis, SMA+$ChAT^{Cre-}$ v SMA+$(Pv+ChAT)^{Cre+}$.

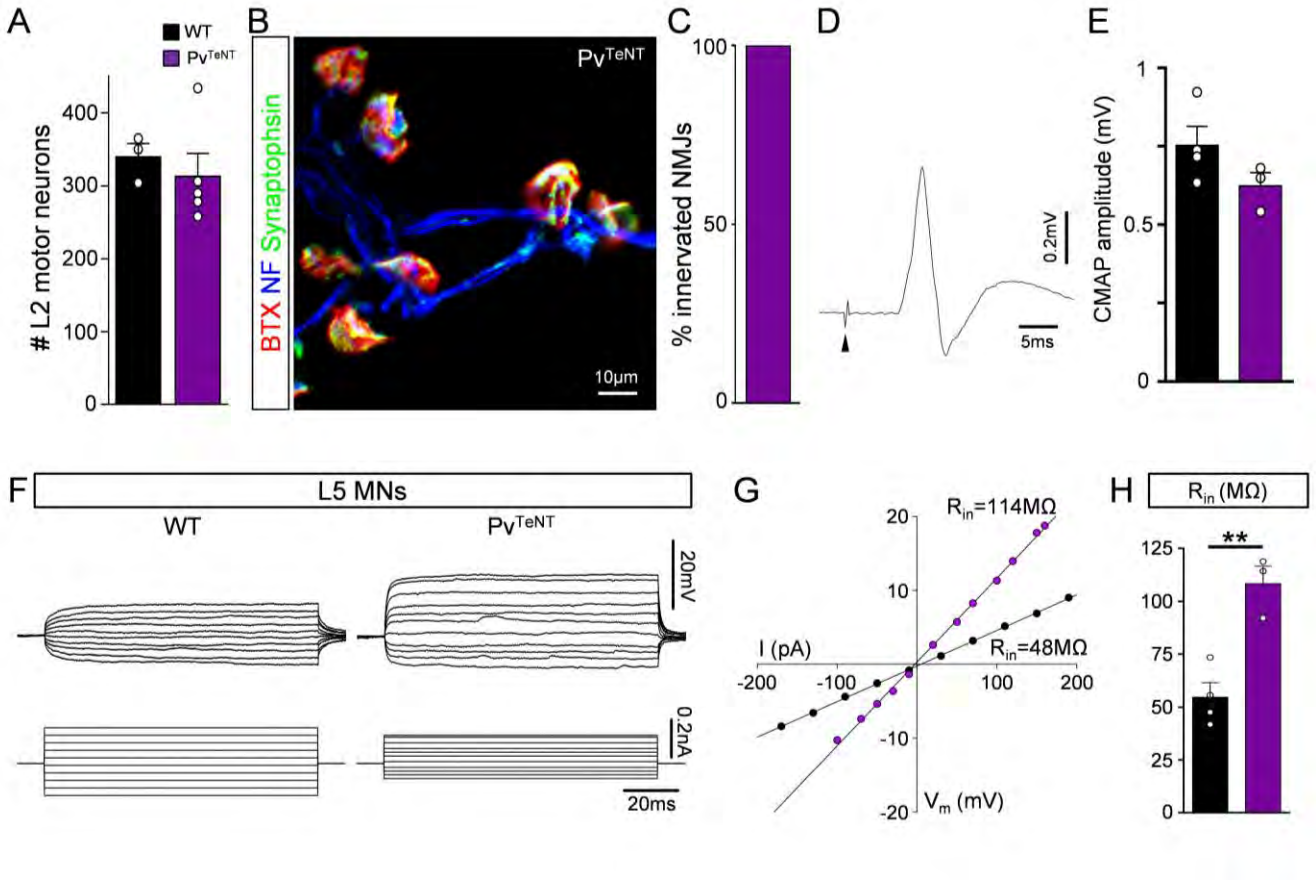

Supplementary Figure 11

Input resistance, motor neuron numbers, NMJ innervation and function in Pv^{TeNT} mice.

(A) Average number of L2 motor neurons in WT and Pv^{TeNT} mice.

(B) Confocal images of NMJs from the QL muscle labeled by the presynaptic markers synaptophysin (green), neurofilament (blue) and the postsynaptic marker bungarotoxin (red) in Pv^{TeNT} mouse at P4.

(C) Percentage of innervation of the QL muscle in Pv^{TeNT} mouse. No denervation was observed.

(D) A compound muscle action potential (CMAP) recorded from the QL muscle following stimulation of the L2 ventral root in a Pv^{TeNT} mouse at P4.

(E) The average peak CMAP amplitude in WT and Pv^{TeNT} mice at P4.

(F) Current-to-voltage relationship in an L5 WT and Pv^{TeNT} motor neurons.

(G) I-V plots for the motor neurons shown in (F).

(H) Average of input resistance for L5 WT (black) and Pv^{TeNT} (purple) motor neurons. ** $p<0.01$, t-test.

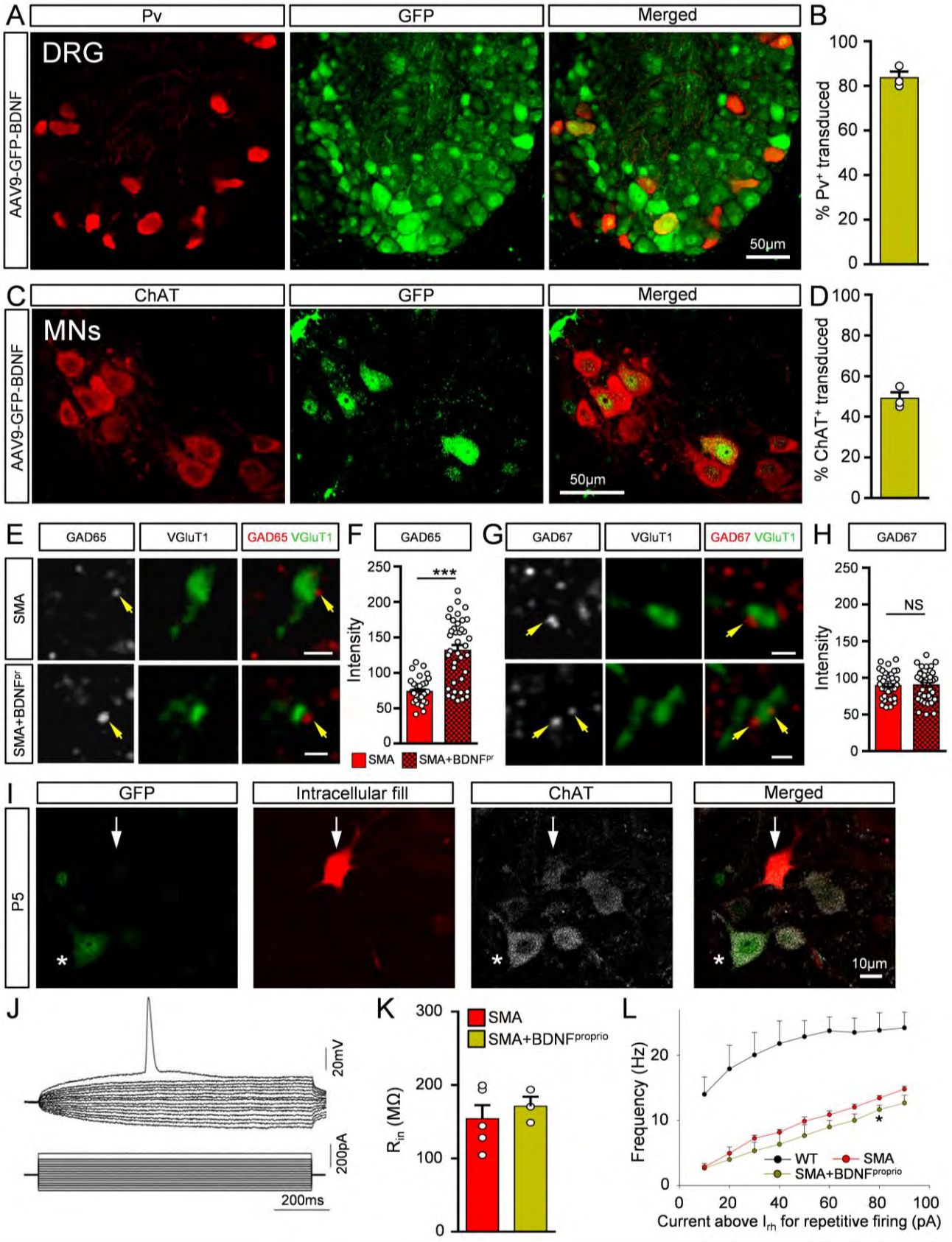

Nature Neuroscience: doi:10.1038/nn.4561

Supplementary Figure 12

Overexpression of BDNF in SMA proprioceptive neurons does not affect the input resistance or firing frequency of SMA motor neurons**.**

(A) Images from L2 DRG (at P5) with parvalbumin (red) and GFP (green) immunoreactivity, following ICV injection with AAV9-GFP-BDNF at P0.

(B) Percentage of parvalbumin+ neurons transduced by AAV9-GFP-BDNF.

(C) Images of ChAT+ motor neurons (red) and GFP (green) following injection with AAV9-GFP-BDNF.

(D) Percentage of motor neurons transduced by AAV9-GFP-BDNF.

(E) Immunoreactivity of GAD65 (red) in GABApre terminals contacting VGluT1 (green) proprioceptive afferent terminals in SMA (top row) and SMA+AAV9-BDNF (bottom row) P5 mice. Yellow arrows indicate GABApre terminals.

(F) Synaptic marker intensity measurements in GAD65+ GABApre terminals at P5. (GAD65: 39 terminals, 3 mice/experimental group). *** P<0.001, Mann-Whitney test.

(G) Immunoreactivity of GAD67 (red) in GABApre terminals contacting VGluT1 (green) proprioceptive afferent terminals in SMA (top row) and SMA+AAV9-BDNF (bottom row) P5 mice. Yellow arrows indicate GABApre terminals.

(H) Synaptic marker intensity measurements (arbitrary units) in GAD67+ GABApre terminals at P5. (GAD67: 39 terminals, 3 mice/experimental group). NS: no significance (P=0.72, Mann-Whitney test).

(I) Intracellular recorded and subsequently filled motor neuron (red) combined with GFP (green) and ChAT (white). Arrow indicates that the recorded motor neuron was not transduced by the virus. Asterisk indicates a nearby transduced motor neuron.

(J) Current to voltage relationship for motor neuron shown in (I).

(K) The average input resistance for 3 non-transduced SMA motor neurons (yellow; SMA+AAV9-BDNF^{proprio}) compared with SMA motor neurons (red; SMA-uninjected).

(L) The firing frequency in 3 non-transduced SMA motor neurons was similar to SMA motor neurons.

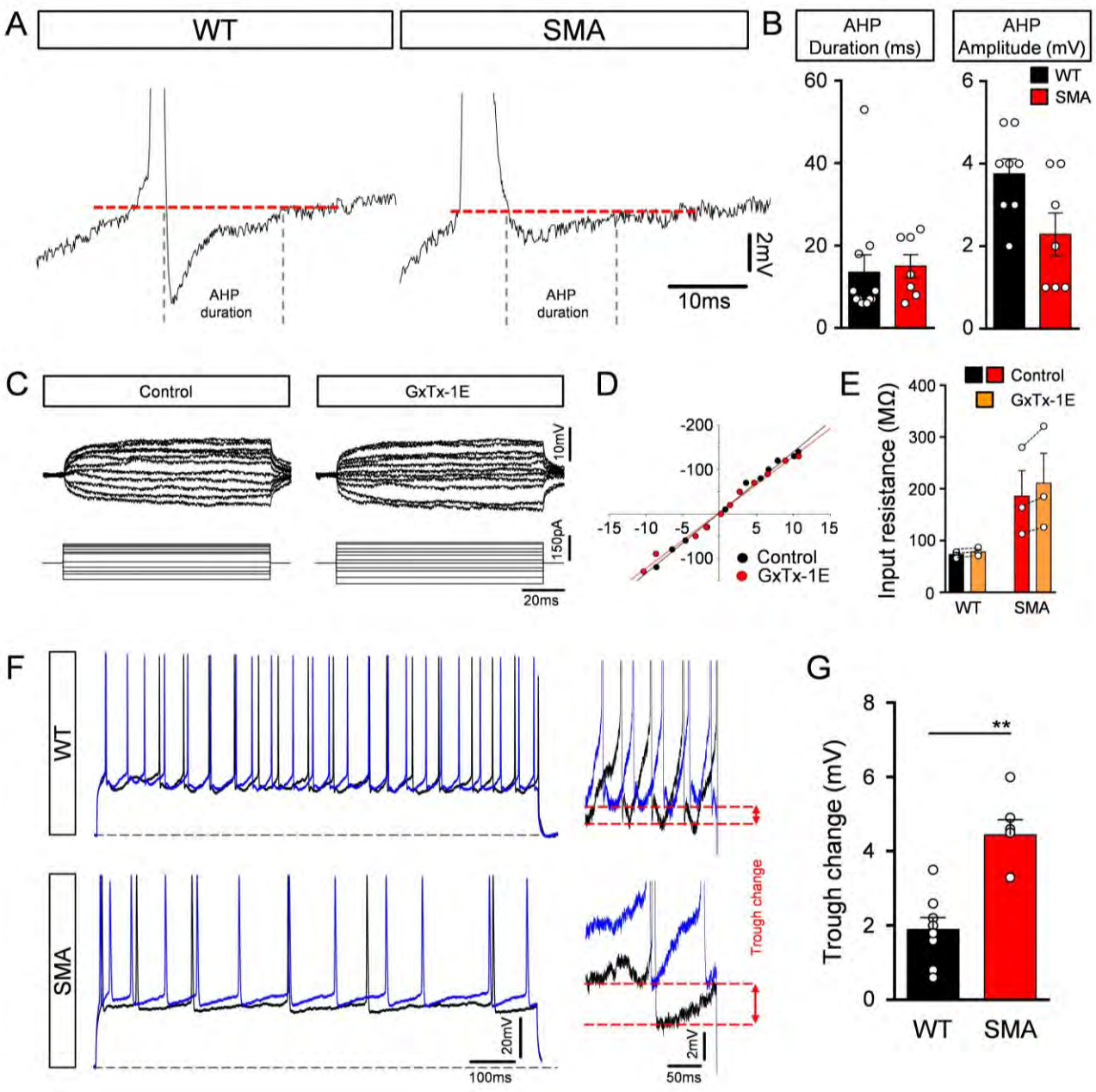

Supplementary Figure 13

Afterhyperpolarization properties, effects of GxTx-1E on input resistance and trough voltage analysis in WT and SMA motor neurons.

(A) Afterhyperpolarization (AHP) in a WT and SMA motor neuron at P4. The AHP was measured from the first action potential evoked following current injection. The AHP duration is indicated between the two grey vertical lines. The AHP amplitude was calculated between the red dotted line (membrane voltage prior to spike initiation) to the peak negative potential.

(B) The average AHP duration (left) and amplitude (right) in WT and SMA motor neurons at P4.

(C) Superimposed membrane responses (top) to current injections (bottom) before and after GxTx-1E exposure.

(D) Current-to-voltage relationship before (black) and after GxTx-1E (red) exposure.

(E) Average values of input resistance before and after GxTx-1E in WT and SMA motor neurons. Lines indicate the change in input

resistance for the individual motor neurons.

(F) Superimposed recordings from repetitive firing at a low frequency (black) and twice that frequency (blue) in a WT (top) and an SMA (bottom) motor neuron. On the right, traces at higher voltage to indicate the change in trough voltage (dotted red lines).

(G) The average trough voltage change in WT (n=8) and SMA (n=6) motor neurons. ** P=0.0023, Mann-Whitney test.

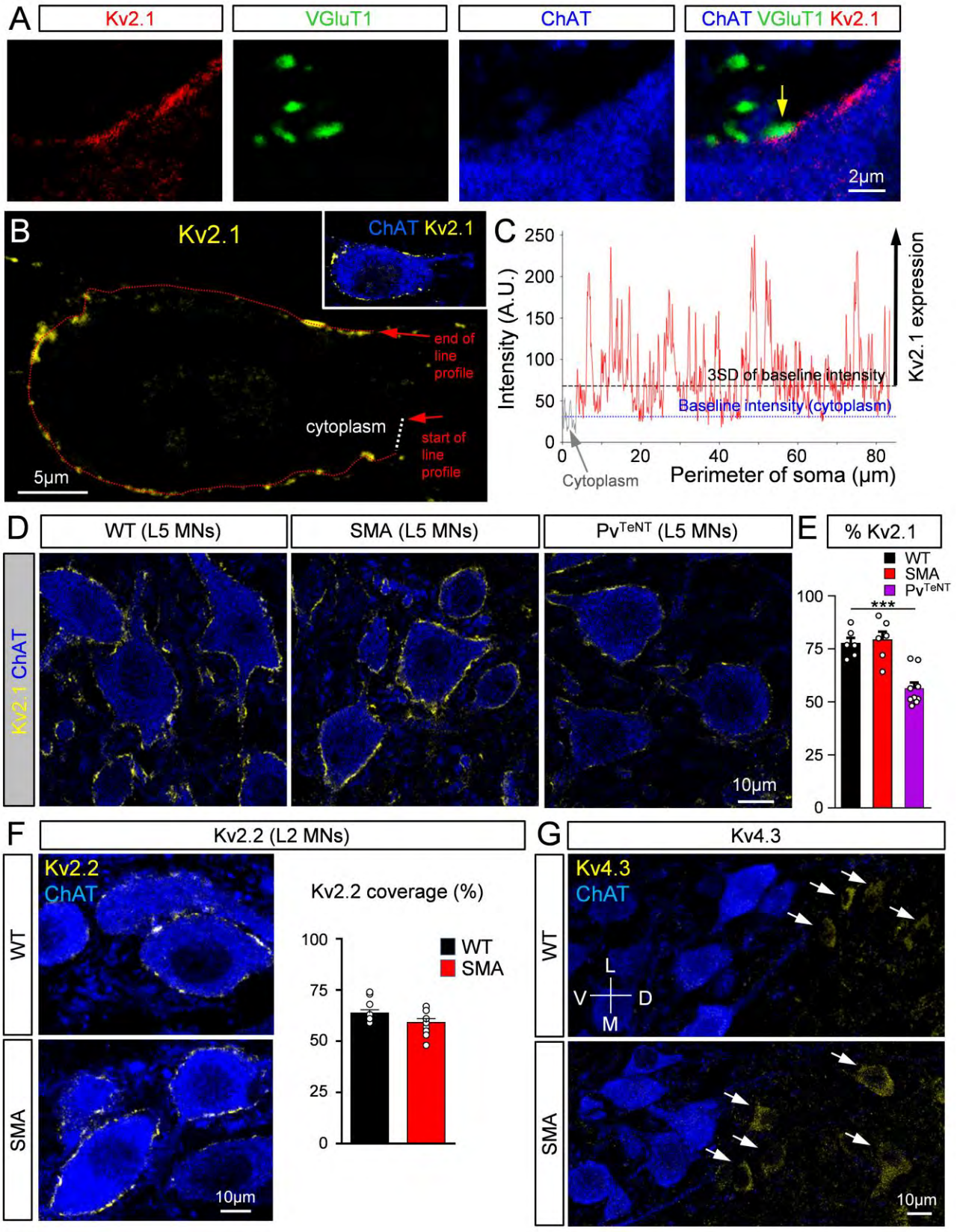

Supplementary Figure 14

Methodology of measuring Kv2.1 surface expression; Kv2.1 in L5 motor neurons in WT, SMA and Pv^{TeNT} motor neurons; Kv2.2 in WT and SMA motor neurons; Kv4.3 expression in WT and SMA mice

(A) Kv2.1 (red), VGluT1 (green), ChAT (blue) immunoreactivity. Yellow arrow indicates the association of a VGluT1+ synapse with post-synaptic Kv2.1 expression.

(B) Analysis of Kv2.1 expression (yellow) was performed from single optical plane images. Only motor neuron somata (inset; ChAT in blue) were analyzed. To calculate the coverage by Kv2.1, a line (red) was drawn along the soma perimeter to acquire the fluorescence intensity. Baseline fluorescence intensity measurement was achieved by drawing a straight line within the cytoplasm (white).

(C) Fluorescence intensity measurement along the perimeter of the motor neuron soma shown in (A). The signal higher than 3 Standard Deviations (black dotted line) of the baseline intensity (blue dotted line) was considered as Kv2.1 expression, while the signal below was considered as background.

(D) Single optical level confocal images of L5 motor neurons (ChAT in blue) expressing Kv2.1 immunoreactivity (yellow) in WT, SMA and Pv^{TeNT} mice at P4.

(E) Percentage somatic coverage of Kv2.1 in L5 WT, SMA and Pv^{TeNT} motor neurons at P4. *** P=0.001, One-Way ANOVA (WT vs Pv^{TeNT} motor neurons).

(F) Single optical plane confocal images of L2 motor neurons (ChAT in blue) expressing Kv2.2 immunoreactivity (yellow) in WT and SMA mice at P4. Graph shows the average percentage somatic coverage of Kv2.2 in L2 WT and SMA motor neurons at P4.

(G) Single optical plane confocal images from an area near the motor neuron nucleus (ChAT in blue) in the L2 spinal segment and Kv4.3 immunoreactivity (yellow) in WT and SMA mice at P4. Kv4.3 was prominently expressed in spinal interneurons (arrows) but not in motor neurons. D: dorsal, V: ventral, L: lateral, M: medial.

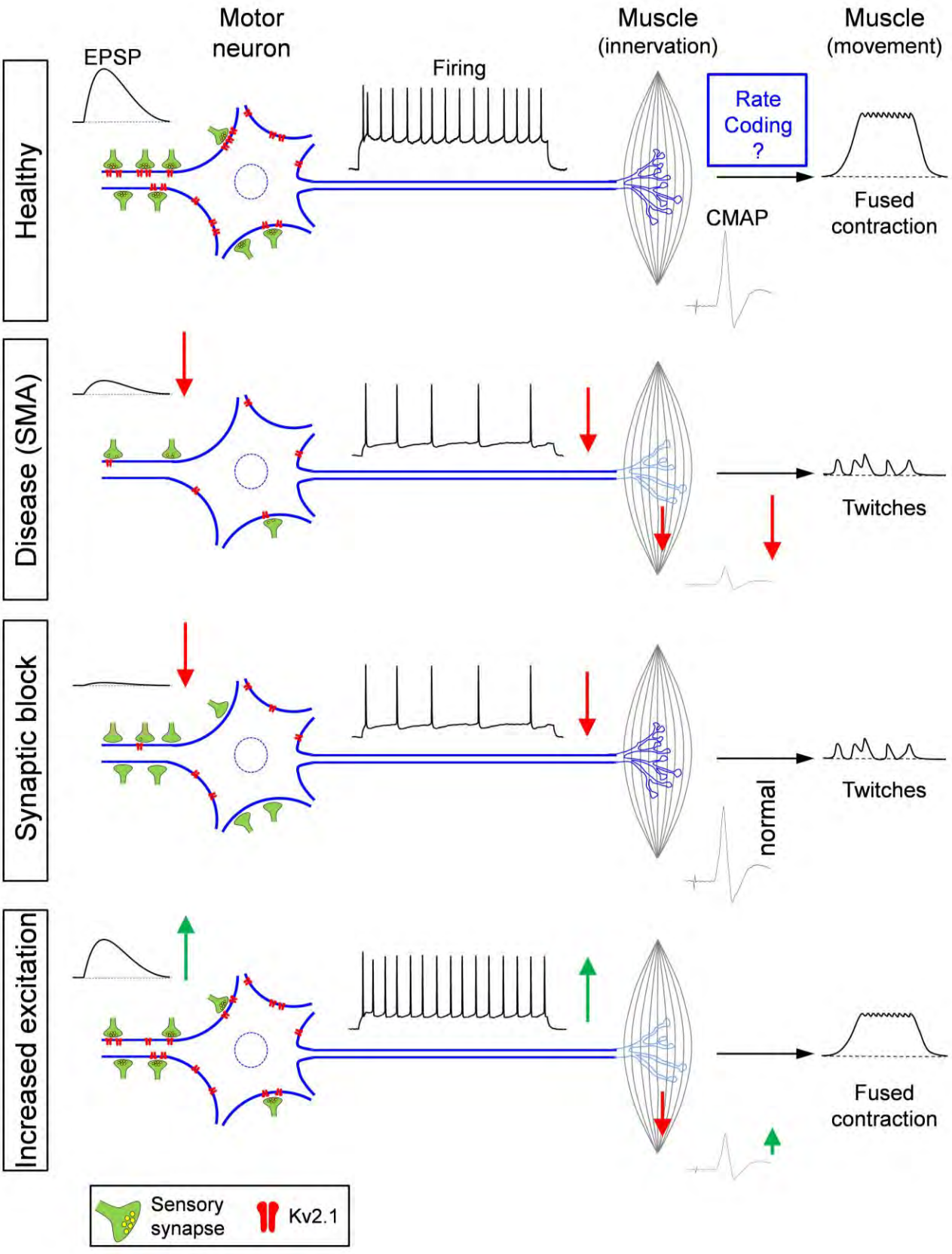

Nature Neuroscience: doi:10.1038/nn.4561

Supplementary Figure 15

Reduced sensory–motor synaptic excitation impairs motor neuron output through the potassium channel Kv2.1

Dysfunction of excitatory proprioceptive synapses caused by disease (SMA) or blocked neurotransmission at sensory-motor synapses, results in reduced excitatory postsynaptic potentials (EPSPs) and subsequently reduced membrane surface expression of Kv2.1 channels on the somata and proximal dendrites of motor neurons. This reduction leads to a significant decrease in the firing frequency of motor neurons. The inability of motor neurons to fire at high frequencies (rate coding) may be a key determinant in muscle contraction. These events can be significantly ameliorated by increasing excitatory synaptic drive (SMA+Pv^{Cre} experiments or treatment of SMA mice with kainate).

Western blots for Fig. 7i

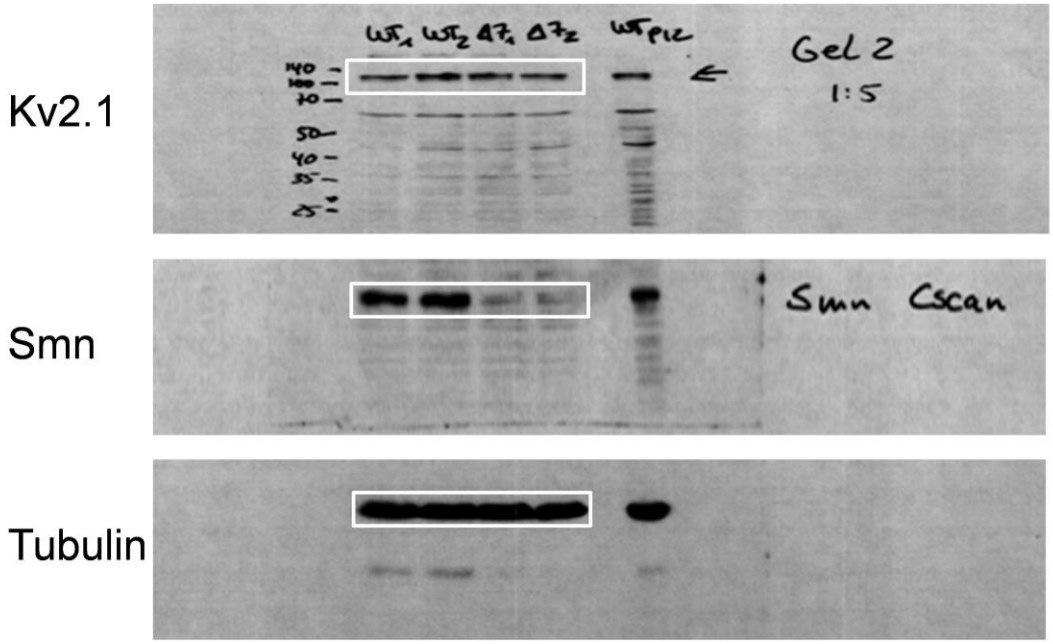

Supplementary Figure 166

Western blots for Figure7i.

Nature Neuroscience: doi:10.1038/nn.4561

Table 1: List of primers used in this study

Allele	mRNA	Oligo	Primers from 5' to 3' seq	Amplicon size (bp)
SMN	Smn^{Res} allele	Sense	ACGCGTACCGTTCGTATAGC	205
		Antisense	TGAGCACCTTCCTTCTTTTTG	
	Smn common primer	Sense	GATGATTCTGACATTTGGGATG	
	Smn	Antisense	TGGCTTATCTGGAGTTTCACAA	325
	Beta Gal (Smn KO)	Antisense	GAGTAACAACCCGTCGGATTC	411
ChAT^{Cre}	WT allele	Sense	GTTTGCAGAAGCGGTGGG	272
	$ChAT^{Cre}$ allele	Sense	TCGCCTTCTTGACGAGTTCTTCTG	350
	Common primer	Antisense	GGCCACTTAGATAGATAATGAGGGGCTC	
PV^{Cre}	WT allele	Antisense	CGAGGGCCATAGAGGATGG	~200
	PV^{Cre} allele	Antisense	GCGGAATTCTTAATTAATCAGCG	~100
	Common primer	Sense	GGATGCTTGCCGAAGATAAGAGTG	

Protocol	Fixation	Preparation	Primary antibody	Secondary antibody	Nuclear stain	Dextran dye
Dual staining for motor neurons and VGluT1	Immersion fixation 4% PFA in PBS 4 hours	Vibratome free-floating; 75 µm	VGluT1 (guinea pig pAb; 1:2000)[1]	Donkey anti-guinea pig-Cy5 IgG (1:250)[2]	-	Dextran Alexa Fluor® 488 in ddH_2O (0.3 mg/10µl)[3]
Triple staining for proprioceptive neurons, SMN, nucleus	Transcardially perfused 2% PFA in sodium acetate buffer pH6 (see Ref 91) with 2 hour post-fixation	Vibratome free-floating; 100 µm	Parvalbumin (chicken pAb; 1:2000)[1]; SMN (mouse mAb; 1:100)[4]	Donkey anti-chicken-Cy3 IgG (1:250)[2]; Donkey anti-mouse-Cy5 IgG (1:250)[2]	DAPI stain (1:10 000)[5]	-
Triple staining for motor neurons, SMN, nucleus	Transcardially perfused 2% PFA in sodium acetate buffer pH6 with 2 hour post-fixation	Vibratome free-floating; 100 µm	ChAT (goat pAb; 1:100)[6]; SMN (mouse mAb; 1:100)[4]	Donkey anti-goat-Cy3 IgG (1:250)[2]; Donkey anti-mouse-Cy5 IgG (1:250)[2]	DAPI stain (1:10 000)[5]	-
Dual staining for motor neurons and proprioceptive neurons	Immersion fixation 4% PFA in PBS 12 hours	Vibratome free-floating; 75 µm	ChAT (goat pA; 1:100)[6]; Parvalbumin (chicken pAb; 1:2000)[1]	Donkey anti-goat-488 IgG (1:250)[2]; Donkey anti-chicken-Cy3 IgG (1:250)[2]	-	-
NMJ triple staining for (presynaptic) motor neuron axon terminal, motor neuron axon, (postsynaptic) acetylcholine nicotinic receptors	Immersion fixation 4% PFA in PBS 20 mins	Muscle whole-mount	Bungarotoxin Alexa Fluor 555 conjugate[3]; Neurofilament (rabbit pAb; 1:500)[6]; Synaptophysin 1 (guinea pig pAb; 1:1000)[7]	Donkey anti-rabbit-488 IgG (1:250)[2]; Donkey anti-guinea pig-Cy5 IgG (1:250)[2]	-	-
Dual staining for motor neurons and $K_v2.1$ channels	Transcardially perfused 2% PFA in sodium acetate buffer pH6 with 2 hour post-fixation	Vibratome free-floating; 100 µm	ChAT (goat pAb; 1:100)[6]; $K_v2.1$ (mouse mAb; 1:2 supernatant clone K89/34)[8]	Donkey anti-goat-Cy3 IgG (1:250)[2]; Donkey anti-mouse-Cy5 IgG (1:250)[2]	-	-
Dual staining for motor neurons and $K_v2.2$ channels	Transcardially perfused 2% PFA in sodium acetate buffer pH6 with 2 hour post-fixation	Vibratome free-floating; 100 µm	ChAT (goat pAb; 1:100)[6]; $K_v2.2$ (mouse mAb; 1:2 supernatant clone N372B/1)[8]	Donkey anti-goat-Cy3 IgG (1:250)[2]; Donkey anti-mouse-Cy5 IgG (1:250)[2]	-	-
Dual staining for motor neurons and $K_v4.3$ channels	Transcardially perfused 2% PFA in sodium acetate buffer pH6 with 2 hour post-fixation	Vibratome free-floating; 100 µm	ChAT (goat pAb; 1:100)[6]; $K_v4.3$ (rabbit pAb; 1:100)[9]	Donkey anti-goat-Cy3 IgG (1:250)[2]; Donkey anti-rabbit-Cy5 IgG (1:250)[2]	-	-
Dual staining for motor neurons and ChAT-Cre	Transcardially perfused 4% PFA in PBS with 4 hour post-fixation	Vibratome free-floating; 100 µm	ChAT (goat pAb; 1:100)[6]; Cre (rabbit pAb; 1:100)[10]	Donkey anti-goat-Cy3 IgG (1:250)[2]; Donkey anti-rabbit-Cy5 IgG (1:250)[2]	-	-
Dual staining for proprioceptive neurons and Parvalbumin-Cre	Transcardially perfused 4% PFA in PBS with 4 hour post-fixation	Vibratome free-floating; 100 µm	Parvalbumin (chicken pAb; 1:2000)[1]; Cre (rabbit pAb; 1:100)[10]	Donkey anti-chicken-Cy3 IgG (1:250)[2]; Donkey anti-rabbit-Cy5 IgG (1:250)[2]	-	-
Dual staining for neuronal brain structures and parvalbumin	Transcardially perfused 4% PFA in PBS with 4 hour post-fixation	Vibratome free-floating; 100 µm	Parvalbumin (chicken pAb; 1:2000)[1]; NeuN (mouse mAb; 1:100)[6]	Donkey anti-chicken-Cy3 IgG (1:250)[2]; Donkey anti-mouse-488 IgG (1:250)[2]	-	-
Staining for parvalbumin in QL and EDL muscles	Transcardially perfused 4% PFA in PBS and 14% (v/v) saturated picric acid with 4 hour post-fixation	Cryostat 20 µm	Parvalbumin (chicken pAb; 1:2000)[1];	Donkey anti-chicken-Cy5 IgG (1:250)[2]	DAPI stain (1:10 000)[5]	-

1. Covance 2. Jackson immuno research 3. Invitrogen 4. BD Biosciences 5. Molecular Probes 6. Millipore 7. Synaptic systems 8. Neuromab 9. Alomone; 10. Gift from Dr Christoph Kellendonk see Ref 56. pAb, polyclonal antibody; mAb, monoclonal antibody; PFA, Paraformaldehyde; PBS, Phosphate-buffered saline; VGluT1, Vesicular glutamate transporter 1; ChAT, Choline acetyltransferase.

Protocol	Fixation	Preparation	Primary antibody	Secondary antibody	Nuclear stain	Dextran dye
Dual staining for motor neurons and VGluT1	Immersion fixation 4% PFA in PBS 4 hours	Vibratome free-floating; 75 µm	VGluT1 (guinea pig pAb; 1:2000)[1]	Donkey anti-guinea pig-Cy5 IgG (1:250)[2]	-	Dextran Alexa Fluor® 488 in ddH_2O (0.3 mg/10µl)[3]
Triple staining for proprioceptive neurons, SMN, nucleus	Transcardially perfused 2% PFA in sodium acetate buffer pH6 (see Ref 91) with 2 hour post-fixation	Vibratome free-floating; 100 µm	Parvalbumin (chicken pAb; 1:2000)[1]; SMN (mouse mAb; 1:100)[4]	Donkey anti-chicken-Cy3 IgG (1:250)[2]; Donkey anti-mouse-Cy5 IgG (1:250)[2]	DAPI stain (1:10 000)[5]	-
Triple staining for motor neurons, SMN, nucleus	Transcardially perfused 2% PFA in sodium acetate buffer pH6 with 2 hour post-fixation	Vibratome free-floating; 100 µm	ChAT (goat pAb; 1:100)[6]; SMN (mouse mAb; 1:100)[4]	Donkey anti-goat-Cy3 IgG (1:250)[2]; Donkey anti-mouse-Cy5 IgG (1:250)[2]	DAPI stain (1:10 000)[5]	-
Dual staining for motor neurons and proprioceptive neurons	Immersion fixation 4% PFA in PBS 12 hours	Vibratome free-floating; 75 µm	ChAT (goat pA; 1:100)[6]; Parvalbumin (chicken pAb; 1:2000)[1]	Donkey anti-goat-488 IgG (1:250)[2]; Donkey anti-chicken-Cy3 IgG (1:250)[2]	-	-
NMJ triple staining for (presynaptic) motor neuron axon terminal, motor neuron axon, (postsynaptic) acetylcholine nicotinic receptors	Immersion fixation 4% PFA in PBS 20 mins	Muscle whole-mount	Bungarotoxin Alexa Fluor 555 conjugate[3]; Neurofilament (rabbit pAb; 1:500)[6]; Synaptophysin 1 (guinea pig pAb; 1:1000)[7]	Donkey anti-rabbit-488 IgG (1:250)[2]; Donkey anti-guinea pig-Cy5 IgG (1:250)[2]	-	-
Dual staining for motor neurons and $K_v2.1$ channels	Transcardially perfused 2% PFA in sodium acetate buffer pH6 with 2 hour post-fixation	Vibratome free-floating; 100 µm	ChAT (goat pAb; 1:100)[6]; $K_v2.1$ (mouse mAb; 1:2 supernatant clone K89/34)[8]	Donkey anti-goat-Cy3 IgG (1:250)[2]; Donkey anti-mouse-Cy5 IgG (1:250)[2]	-	-
Dual staining for motor neurons and $K_v2.2$ channels	Transcardially perfused 2% PFA in sodium acetate buffer pH6 with 2 hour post-fixation	Vibratome free-floating; 100 µm	ChAT (goat pAb; 1:100)[6]; $K_v2.2$ (mouse mAb; 1:2 supernatant clone N372B/1)[8]	Donkey anti-goat-Cy3 IgG (1:250)[2]; Donkey anti-mouse-Cy5 IgG (1:250)[2]	-	-
Dual staining for motor neurons and $K_v4.3$ channels	Transcardially perfused 2% PFA in sodium acetate buffer pH6 with 2 hour post-fixation	Vibratome free-floating; 100 µm	ChAT (goat pAb; 1:100)[6]; $K_v4.3$ (rabbit pAb; 1:100)[9]	Donkey anti-goat-Cy3 IgG (1:250)[2]; Donkey anti-rabbit-Cy5 IgG (1:250)[2]	-	-
Dual staining for motor neurons and ChAT-Cre	Transcardially perfused 4% PFA in PBS with 4 hour post-fixation	Vibratome free-floating; 100 µm	ChAT (goat pAb; 1:100)[6]; Cre (rabbit pAb; 1:100)[10]	Donkey anti-goat-Cy3 IgG (1:250)[2]; Donkey anti-rabbit-Cy5 IgG (1:250)[2]	-	-
Dual staining for proprioceptive neurons and Parvalbumin-Cre	Transcardially perfused 4% PFA in PBS with 4 hour post-fixation	Vibratome free-floating; 100 µm	Parvalbumin (chicken pAb; 1:2000)[1]; Cre (rabbit pAb; 1:100)[10]	Donkey anti-chicken-Cy3 IgG (1:250)[2]; Donkey anti-rabbit-Cy5 IgG (1:250)[2]	-	-
Dual staining for neuronal brain structures and parvalbumin	Transcardially perfused 4% PFA in PBS with 4 hour post-fixation	Vibratome free-floating; 100 µm	Parvalbumin (chicken pAb; 1:2000)[1]; NeuN (mouse mAb; 1:100)[6]	Donkey anti-chicken-Cy3 IgG (1:250)[2]; Donkey anti-mouse-488 IgG (1:250)[2]	-	-
Staining for parvalbumin in QL and EDL muscles	Transcardially perfused 4% PFA in PBS and 14% (v/v) saturated picric acid with 4 hour post-fixation	Cryostat 20 µm	Parvalbumin (chicken pAb; 1:2000)[1];	Donkey anti-chicken-Cy5 IgG (1:250)[2]	DAPI stain (1:10 000)[5]	-

1. Covance 2. Jackson immuno research 3. Invitrogen 4. BD Biosciences 5. Molecular Probes 6. Millipore 7. Synaptic systems 8. Neuromab 9. Alomone; 10. Gift from Dr Christoph Kellendonk (Columbia University) . pAb, polyclonal antibody; mAb, monoclonal antibody; PFA, Paraformaldehyde; PBS, Phosphate-buffered saline; VGluT1, Vesicular glutamate transporter 1; ChAT, Choline acetyltransferase.

Nature Neuroscience: doi:10.1038/nn.4561

Secondary antibodies	**Source**	**Catalog number**
Donkey anti-guinea pig-Cy5 IgG	Jackson Immunoresearch	706-175-148
Donkey anti-mouse-Cy5 IgG	Jackson Immunoresearch	715-175-151
Donkey anti-chicken-Cy5 IgG	Jackson Immunoresearch	703-175-155
Donkey anti-rabbit-Cy5 IgG	Jackson Immunoresearch	711-175-152
Donkey anti-chicken-Cy3 IgG	Jackson Immunoresearch	703-545-155
Donkey anti-goat-Cy3 IgG	Jackson Immunoresearch	705-165-147
Donkey anti-goat-488 IgG	Jackson Immunoresearch	705-545-003
Donkey anti-rabbit-488 IgG	Jackson Immunoresearch	711-545-152
Donkey anti-mouse-488 IgG	Jackson Immunoresearch	715-545-150
Streptavidin, Alexa Fluor- 488	Molecular Probes	S11223

Primary antibodies		
Parvalbumin (chicken)	Covance	AP37-47
SMN (mouse)	BD Biosciences	610646
ChAT (goat)	Millipore	AB144P
Bungarotoxin Alexa Fluor 555 conjugate	Invitrogen	B35451
Neurofilament (rabbit)	Millipore	AB1987
Synaptophysin (guinea pig)	Synaptic systems	101-004
Kv2.1 (mouse mAb clone K89/34)	NeuroMab	73-014
Kv2.2 (mouse mAb; 1:2 clone N372B/1)	NeuroMab	73-369
Kv4.3 (rabbit)	Alomone	APC-017
NeuN (mouse)	Millipore	MAB377
GFP (chicken)	Abcam	ab13970
DAPI stain	Molecular Probes	D3571